Check for updates

ADVANCED MATERIALS
www.advmat.de

Proteolysis-triggered RNA Interference for Mitochondrial Iron Dyshomeostasis to Activate Antitumor Immunity in Hepatic Carcinoma

Shi-Man Zhang, Xiao-Kang Jin, Hong Chen, Yu-Zhang Wang, Jun-Long Liang, Jun Feng, Wei-Hai Chen, and Xian-Zheng Zhang**

Although the disturbance of iron metabolism holds significant promise for antitumor therapy, the specific regulation of the precise acting site remains challenging. Here, a self-triggering proteolysis RNA interference system (cRGD-VFs) is elaborately constructed to precisely disturb mitochondrial iron homeostasis, the core hub of cellular iron regulation, for evoking antitumor immunity. Specifically, ferritin is conjugated with E3 ligase ligand VH032 and tumor-targeting cRGD peptide through click chemistry, and further loaded with ENO1-targeted siRNA to prepare cRGD-VFs. Following the targeted uptake by tumor cells, cRGD-VFs recruits E3 ligase to initiate the ubiquitination process to trigger the proteolysis of ferritin, resulting in the release of abundant Fe^{2+} and the loaded siRNA. siRNA-mediated ENO1-targeted knockdown would upregulate the mitochondrial iron transport channel through the ENO1-IRP1-Mfrn1 pathway, which subsequently leads to mitochondrial iron overload and the increase of detrimental mitochondrial reactive oxygen species (ROS), thereby triggering severe mitochondria destruction and causing mass death of tumor cells. Noteworthily, it is found that cRGD-VFs-mediated mitochondrial iron overload can activate powerful antitumor immunity by upregulating immune-related pathways to eliminate tumors, achieving notable tumor suppression in multiple murine liver cancer models, which represents a promising strategy of disturbing mitochondrial iron homeostasis for potentiating antitumor immunotherapy.

1. Introduction

Iron is an essential microelement for cellular activities, and tumor cells live with a keen demand of iron to meet the needs of malignant proliferation and growth.[1,2] Abnormal iron metabolism would irreversibly induce cell death, rendering iron metabolism as a vital therapeutic target of cancer.[3,4] For instance, excessive iron in tumor cells leads to the perturbation of intracellular iron homeostasis, causing cell death by severe oxidative stress via Fe^{2+}-mediated Fenton reaction.[5–7] However, tumor cells have been demonstrated to develop tolerance against iron-related cell death via activating the self-protection mechanism, resulting in the increasing intractability of cancer treatment.[8–10] Moreover, the current iron-related therapies mainly target or modulate the iron content at the cellular level or in the tumor microenvironment, rather than the key regulatory center of iron metabolism.[11–13] Thus, a more precise approach, focusing on the specific regulation of the precise acting site of iron homeostasis, is urgently needed to potentiate the antitumor efficacy of iron-related tumor therapy.

It is well noted that mitochondria are closely implicated in multiple cellular homeostasis regulation of tumor cells, typically iron homeostasis.[14–16] In mitochondria, iron acts as an important prosthetic group in the synthetic process of multiple key enzymes, such as cytochrome and iron-sulfur protein, which are essential for bioenergetic and biosynthetic needs.[17] Since mitochondria occupy a pivotal role in the cellular metabolism and bioenergetics, tumor cells are susceptible to lethal damage induced by irreversible mitochondrial destruction.[18–20] Moreover, the deepening understanding towards cell biology and immunology highlights the role of mitochondria in enhancing tumor immunogenicity.[21] Mitochondria contain a variety of immune-stimulating factors, which could be liberated upon mitochondrial dysfunction and trigger the downstream immune responses.[22–25] These characteristics enlighten the exploitation of mitochondria-targeted immunotherapy,[26–28] while the targeted regulation of mitochondrial iron homeostasis for antitumor immunotherapy remains challenging.

Recently, α-enolase (ENO1) has been discovered to regulate mitochondrial iron homeostasis to resist tumor ferroptosis.[29] Tumor cells upregulate ENO1 to facilitate the mRNA degradation

---

S.-M. Zhang, X.-K. Jin, H. Chen, Y.-Z. Wang, J.-L. Liang, J. Feng,
W.-H. Chen, X.-Z. Zhang
Key Laboratory of Biomedical Polymers of Ministry of Education &
Department of Chemistry
Department of Cardiology
Zhongnan Hospital
Wuhan University
Wuhan 430072, P. R. China
E-mail: chenweihai@whu.edu.cn; xz-zhang@whu.edu.cn

The ORCID identification number(s) for the author(s) of this article can be found under https://doi.org/10.1002/adma.202508457

DOI: 10.1002/adma.202508457

© 2025 Wiley-VCH GmbH

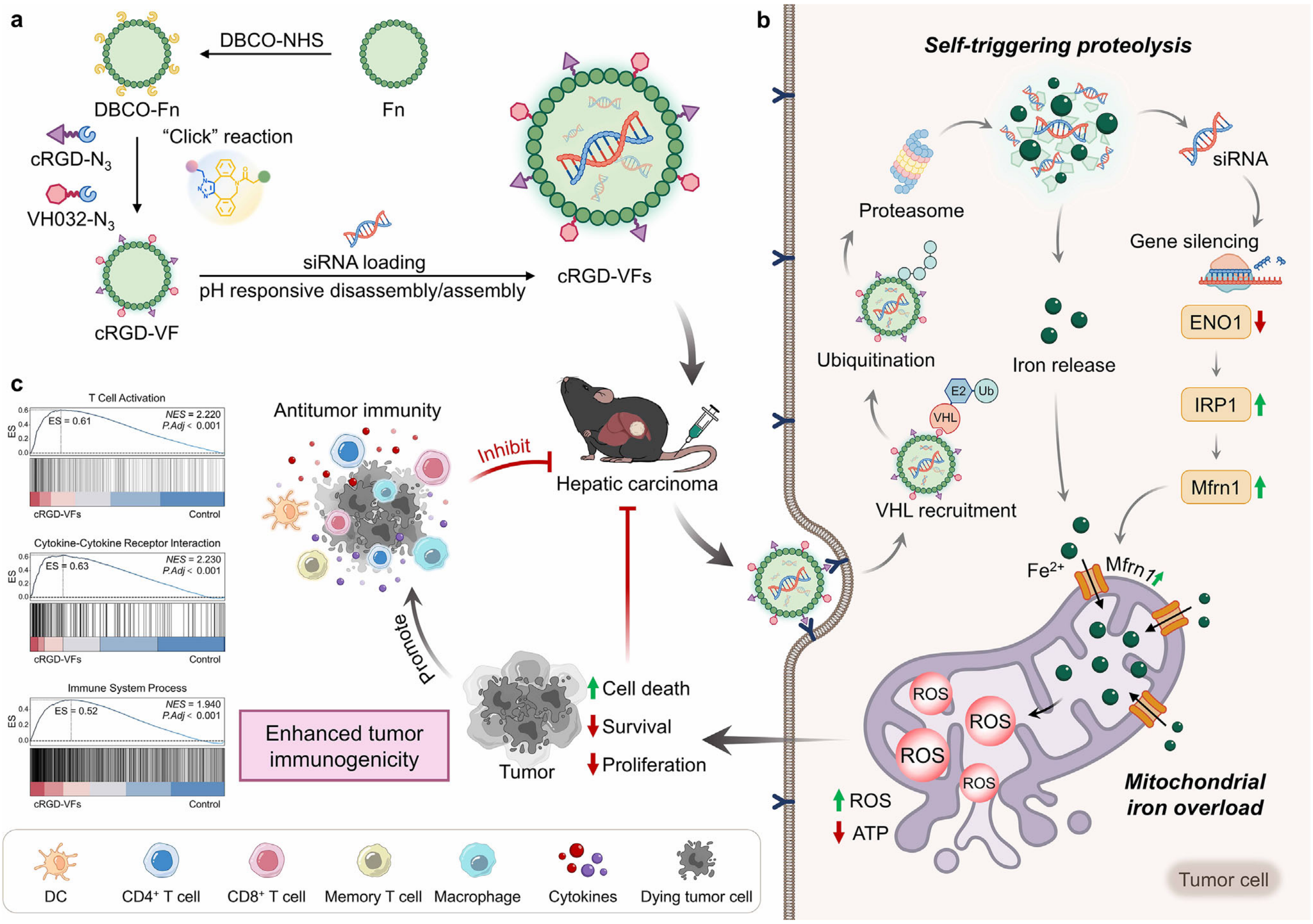

Scheme 1. Schematic illustration of cRGD-VFs-mediated mitochondrial iron homeostasis disturbance for antitumor immunotherapy. a) The detailed preparation process of cRGD-VFs. b) The mechanism of cRGD-VFs-mediated mitochondrial iron overload to induce tumor cell death. c) cRGD-VFs enhanced tumor immunogenicity and initiated antitumor immunity to eliminate tumors.

of iron regulatory protein 1 (IRP1), which further inhibits the expression of mitoferrin-1 (Mfrn1). The downregulated Mfrn1 would tighten the mitochondrial iron flux to protect mitochondria from iron-related damage, thereby resulting in resistance towards iron-related tumor cell death. This inspire that the direct disturbance of mitochondrial iron homeostasis would be more effective in destroying mitochondria for tumor killing. Therefore, efficient methods are needed for acute iron stress to induce mitochondrial iron dyshomeostasis in tumor cells. Naturally, ferritin is ideal for iron supply as a ubiquitous iron storage protein. However, ferritin displays very prominent acid-base tolerance and hardly releases iron in physiological conditions.[30,31] Moreover, tumor cells have developed complex and rigorous mechanisms to maintain intracellular iron balance and merely release free iron through ferritinophagy under iron depletion.[32,33] Of particular importance, the development of targeted protein degradation (TPD), typically proteolysis targeting chimeras (PROTACs), inspires the utilization of the ubiquitin-proteasome system (UPS) in liberating iron ions from ferritin.[34–36] By directing the bonding of ferritin to UPS, the chelated iron ions in ferritin can be efficiently released, thus significantly increasing the free iron in tumor cells and providing a golden opportunity for mitochondrial iron overload.

Here, a self-triggering proteolysis RNA interference system was rationally designed for mitochondrion-targeted iron homeostasis regulation to activate antitumor immunity. Specifically, the E3 ligase ligands VHL032 and tumor-targeting cyclo-RGDfK (cRGD) peptides were conjugated to ferritin through click reaction (**Scheme 1**). ENO1-targeted siRNA was subsequently loaded into the protein vector based on the pH-dependent depolymerization/reassembly characteristic of ferritin. The constructed cRGD-VFs displayed a structure analogous to proteolysis-targeting chimaeras, and innovatively utilized the natural UPS to degrade the ferritin for the release of iron ions and ENO1-targeted siRNA. By interfering with its transcription, the expression of ENO1 was downregulated to modulate the ENO1-IRP1-Mfrn1 pathway, and eventually upregulate the expression of Mfrn1 to increase mitochondrial iron transport channels. Particularly, the influx of mitochondrial iron was significantly enhanced and promoted the accumulation of active iron in mitochondria, resulting in excessive production of toxic reactive oxygen species (ROS) to induce mitochondrial dysfunction. Thus, the collapse of mitochondria interfered with the redox homeostasis throughout the cell and eventually initiated tumor cell death. Notably, cRGD-VFs-mediated mitochondrial iron overload could activate powerful antitumor immunity by upregulating immune-related pathways to eliminate

© 2025 Wiley-VCH GmbH

15214095, 0, Downloaded from https://advanced.onlinelibrary.wiley.com/doi/10.1002/adma.202508457 by University Of British Columbia, Wiley Online Library on [01/09/2025]. See the Terms and Conditions (https://onlinelibrary.wiley.com/terms-and-conditions) on Wiley Online Library for rules of use; OA articles are governed by the applicable Creative Commons License

tumors, achieving notable tumor suppression in multiple murine liver cancer models, which provided insights into developing therapeutic strategies for disturbing mitochondrial iron homeostasis in cancer immunotherapy.

2. Results and Discussion

2.1. High-Expressed ENO1 Corelated with the Poor Prognosis of Liver Cancer

The higher expression of ENO1 has been found in several malignancies as analyzed from the Cancer Genome Atlas (TGCA), especially for liver hepatocellular carcinoma (LIHC) (**Figures** 1a and S1, Supporting Information), which is considered as a typical tumor marker. In liver cancer, the overexpressed ENO1 correlates with the poor overall survival (Figure 1b), demonstrating the promising potential of ENO1 suppression in inhibiting tumor progress. It has been reported that ENO1 as a critical glycolytic enzyme, sustains tumor proliferation and promotes the invasion and metastasis of tumor cells[37,38] while the role of ENO1 in regulating tumor iron homeostasis has been recently discovered.[29] In tumor cells, ENO1 could function as an RNA degradosome to degrade IRP1 mRNA, whereas IRP1 is involved in the post-transcriptional regulation of multiple genes related to the intracellular iron influx, storage, and efflux, serving as a pivot in regulating cellular iron metabolism.[39,40] And ENO1-mediated IRP1 inhibition would further result in the downregulation of Mfrn1, thus leading to the impaired mitochondrial iron influx and protecting tumor cells from mitochondrial iron-related oxidative stress. The lower level of Mfrn1 in tumor tissues than that of noncancerous tissues reveals its possible function as a tumor suppressor (Figure 1c). The ENO1-IRP1-Mfrn1 pathway is considered to sustain cellular iron balance, specifically mitochondrial iron homeostasis, and saves tumor cells from ferroptotic death. Particularly, ENO1-targeted siRNA (siENO1) was elaborately designed, which exhibited 61.7% downregulation of ENO1 mRNA expression in tumor cells as compared to the control (Figure S2, Supporting Information), while the scramble siRNA did not significantly inhibit ENO1 mRNA expression, verifying that siENO1 could silence ENO1 expression in a highly sequence-specific manner. It was found that the knockdown of ENO1 by siRNA could improve the mRNA level of IRP1 (Figure 1d,e), and further resulted in the upregulated expression of Mfrn1 in tumor cells. Collectively, these results indicated that interference with the ENO1-IRP1-Mfrn1 axis would accelerate iron enrichment in mitochondria, improve the sensitivity of tumor cells to mitochondrial iron overload, and eventually lead to tumor death.

2.2. Construction and Characterization of Proteolysis-Initiated RNA Interference System

Initially, ferritin (Fn) was labelled with dibenzocyclooctyne (DBCO) group via amidation (Figure 1f). Then, VHL ligands VH032 and tumor-targeting cRGD peptides were successively conjugated with DBCO-labelled Fn through click reaction to form cRGD-VF before loading siRNA. In detail, the grafting rate of VH032 and cRGD was 14.8% and 8.4%, respectively, as detected by high performance liquid chromatography (HPLC) (Figures S3 and S4, Supporting Information). As observed with transmission electron microscopy (TEM), the unmodified Fn displayed cage-like structure with a uniform size of ≈14.8 nm, while surface modification of VH032 and cRGD did not significantly change the morphology but resulted in a larger hydrated size of ≈16.3 nm as measured by dynamic light scattering (DLS) (Figure 1g,h). Moreover, the pH-responsive disassembly/reassembly characteristic of ferritin nanocage was diligently examined. TEM images showed the depolymerization of Fn and cRGD-VF into protein subunits at pH 2, displaying as the irregular fragments (Figure S5, Supporting Information). When pH was adjusted from acidic back to 7, the reassembly of Fn into a cage-like structure was clearly observed, so did cRGD-VF. The reversible self-assembly ability of cRGD-VF set the stage for the subsequent siRNA loading. After loading ENO1-targeted siRNA, the engineered RNA interference system (cRGD-VFs) was successfully obtained. As displayed in Figure 1g, cRGD-VFs displayed spherical morphology, and the cavity of ferritin was filled. DLS analysis showed that the hydrated size of cRGD-VFs was enlarged to ≈65.5 nm with a negative zeta potential of -12.7 mV (Figure 1h,i). The encapsulation efficiency was further detected under different molar ratios of Fn to siRNA by agarose gel electrophoresis (AGE). As the molar ratio increased from 1 : 1 to 10 : 1, the encapsulation efficiency of siRNA significantly enhanced from 13.9% to 72.2% (Figure 1j and Figure S6, Supporting Information). However, when the ratio was further elevated to 15 : 1, the encapsulation efficiency was reduced to 47.7%. Thus, the optimal molar ratio of Fn to siRNA was selected at 10 : 1 for the construction of cRGD-VFs. Particularly, the ferritin shell could protect the inside loading siRNA from the degradation of RNase A (Figure 1k). Moreover, under pH 6.5, cRGD-VF retained a well-defined cage-like structure, while cRGD-VFs also maintained structural integrity without noticeable alteration in morphology, indicating the favorable stability of cRGD-VF and cRGD-VFs within the tumor microenvironment (Figure S7, Supporting Information). These promise the integrity of siRNA to bring out the effective RNA interference for perturbing mitochondrial iron homeostasis.

2.3. cRGD-VFs Induced Mitochondrial Dysfunction Through Mitochondrial Iron Overload

Cellular uptake of the constructed cRGD-VFs was examined by confocal microscopy observation and flow cytometric analysis. As shown in **Figure** 2a, Fs (siRNA-loaded Fn) exhibited slightly better cellular internalization as compared to VFs (siRNA-loaded VH032-modified Fn) within the first 2 h. In comparison, Hepa1-6 murine hepatoma cells treated with cRGD-VFs displayed stronger red fluorescence than that of Fs and VFs. After coculture for 4 and 6 h, Fs and VFs displayed the comparable extent of intracellular uptake, while the functionalization of cRGD peptide offered cRGD-VFs a significantly higher tropism toward tumor cells (Figure S8, Supporting Information). As a hyperperfusion organ, the liver with an abundant mononuclear phagocyte system is generally considered as the main biological barrier for intravenous drug delivery. Particularly, the liver tends to intercept and eliminate most circulatory foreign nanoparticles and therefore prevents the effective accumulation of nanoparticles at the

© 2025 Wiley-VCH GmbH

15214095, 0, Downloaded from https://advanced.onlinelibrary.wiley.com/doi/10.1002/adma.202508457 by University Of British Columbia, Wiley Online Library on [01/09/2025]. See the Terms and Conditions (https://onlinelibrary.wiley.com/terms-and-conditions) on Wiley Online Library for rules of use; OA articles are governed by the applicable Creative Commons License

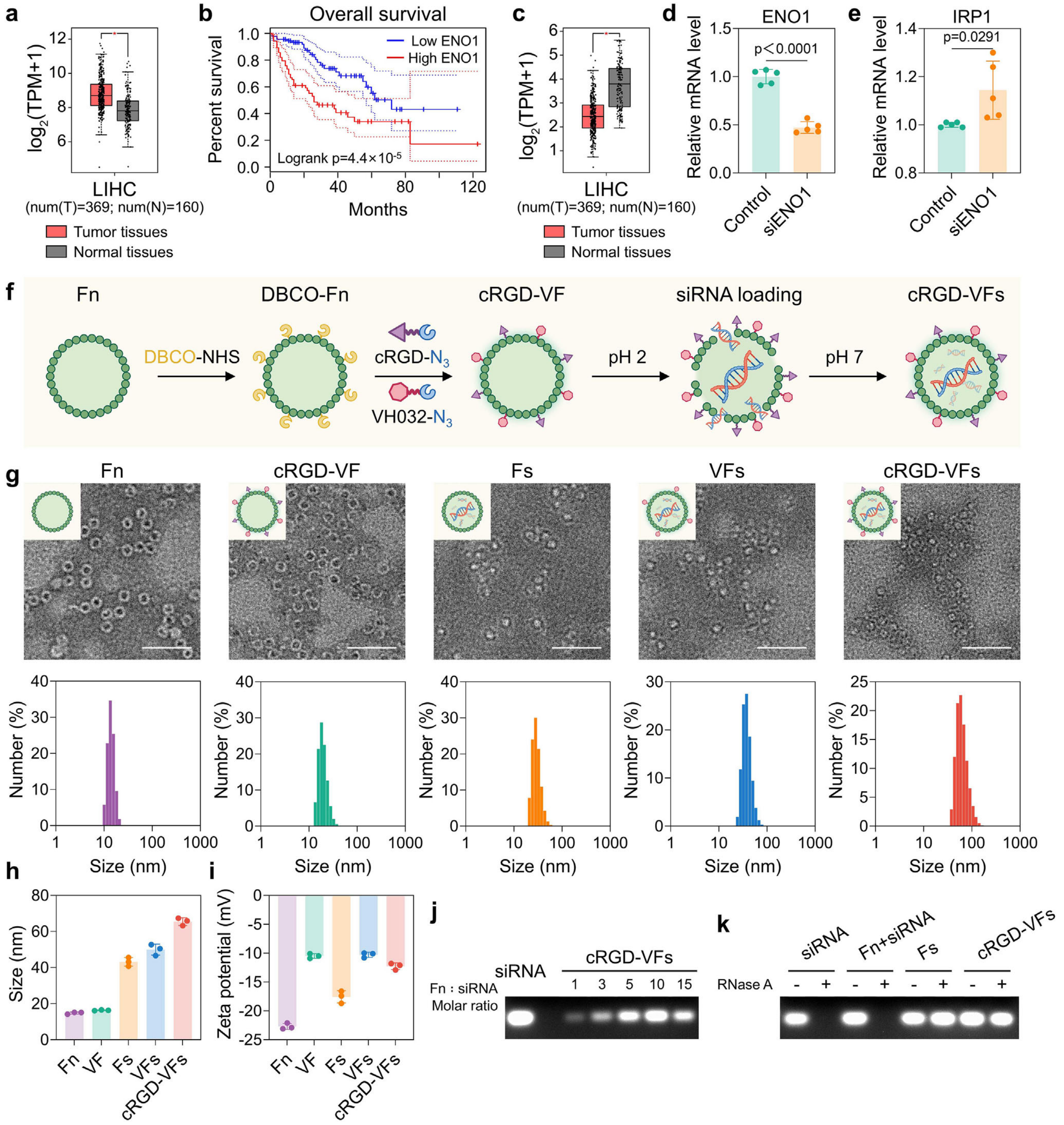

Figure 1. Characterization of cRGD-VFs. a) ENO1 gene expression in liver cancer and paired normal tissues. b) Overall survival of LIHC patients with high or low ENO1 expression. c) Mfrn1 gene expression in liver cancer and paired normal tissues. Data in Figure a–c were analyzed on TGCA. d) ENO1 mRNA level change in tumor cells treated with ENO1-targeted siRNA (siENO1). e) IRP1 mRNA level change in tumor cells treated with siENO1. f) The preparation process of cRGD-VFs. g) Representative TEM images of Fn, cRGD-VF, Fs, VFs, and cRGD-VFs, respectively, and the corresponding hydrodynamic sizes of Fn, cRGD-VF, Fs, VFs, and cRGD-VFs analyzed by DLS. h) Average diameters of different nanoparticles. i) Zeta potential of different nanoparticles. j) Evaluation of the encapsulation efficiency under different ratios of ferritin to siRNA. k) Evaluation of the stability of siRNA after cocultured with RNase A. $n = 5$ biologically independent samples in Figure d,e. Statistical significance in Figure d, e was calculated by an unpaired t-test.

15214095, 0, Downloaded from https://advanced.onlinelibrary.wiley.com/doi/10.1002/adma.202508457 by University Of British Columbia, Wiley Online Library on [01/09/2025]. See the Terms and Conditions (https://onlinelibrary.wiley.com/terms-and-conditions) on Wiley Online Library for rules of use; OA articles are governed by the applicable Creative Commons License

15214095, 0, Downloaded from https://onlinelibrary.wiley.com/doi/10.1002/adma.202508457 by University Of British Columbia, Wiley Online Library on [01/09/2025]. See the Terms and Conditions (https://onlinelibrary.wiley.com/terms-and-conditions) on Wiley Online Library for rules of use; OA articles are governed by the applicable Creative Commons License

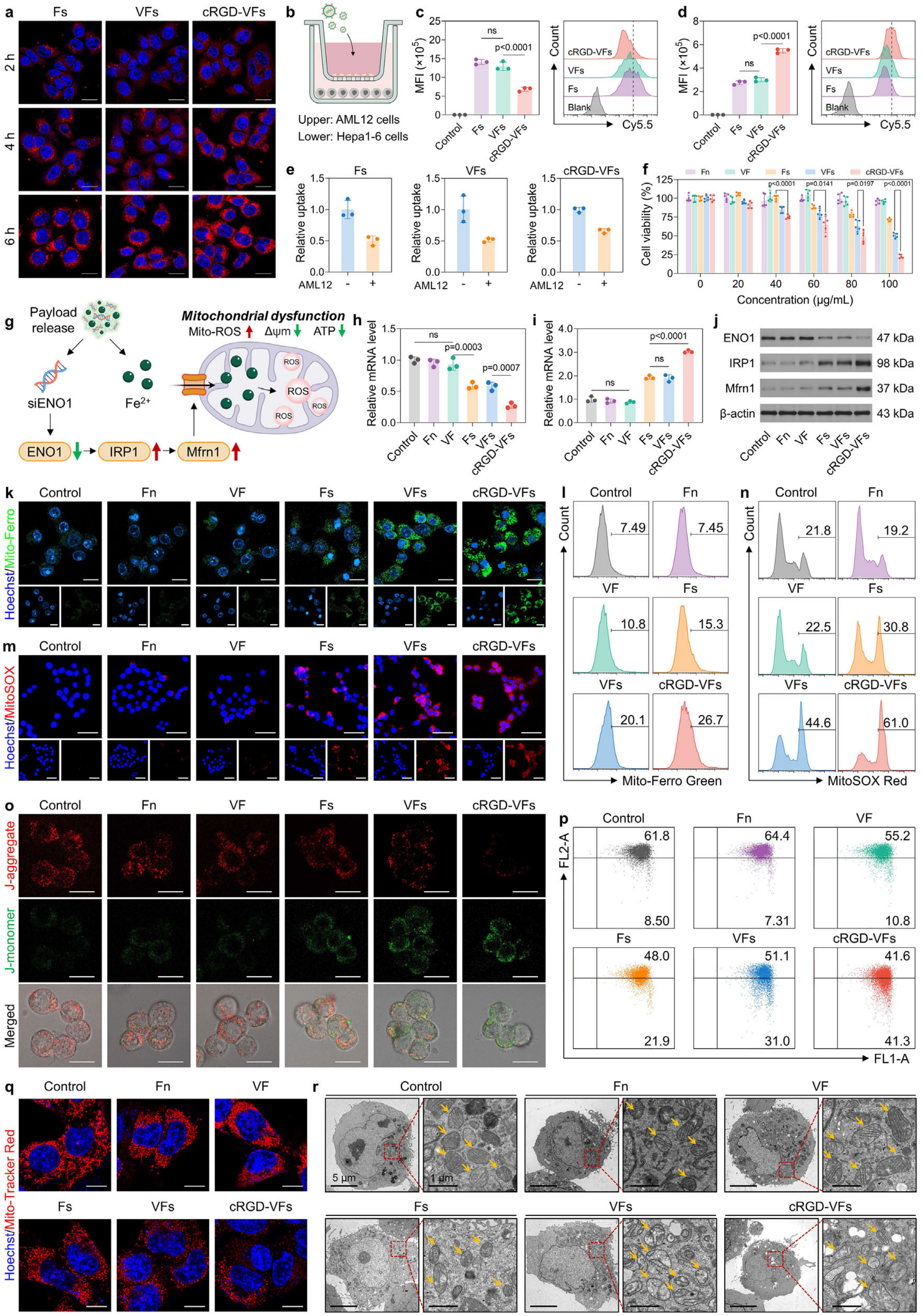

Figure 2. Evaluation of mitochondrial dysfunction induced by cRGD-VFs. a) CLSM images of Hepa1-6 tumor cells treated with Cy5.5-labelled Fs, VFs, and cRGD-VFs. Scale bar: 10 μm. b) Schematic illustration of the transwell assay in the simulation of the interception by liver cells in vitro. c) MFI of AML12 liver cells treated with Fs, VFs, and cRGD-VFs and the corresponding flow cytometric analysis. d) MFI of Hepa1-6 tumor cells treated with Fs, VFs, and cRGD-VFs and the corresponding flow cytometric analysis. e) The uptake efficiency of Fs, VFs and cRGD-VFs by Hepa1-6 tumor cells with and

© 2025 Wiley-VCH GmbH

lesion site, which greatly limits the therapeutic effects. Thus, a transwell assay was conducted to study whether the modification of cRGD peptides could help ferritin-based vectors to circumvent the interception of liver cells (Figure 2b). Results of flow cytometry detection showed that Fs and VFs displayed limited capability to escape from the capture of hepatocytes, as demonstrated by the comparatively higher fluorescence signal in AML12 normal liver cells (Figure 2c,d). Correspondingly, the setup of AML12 cells on the upper chamber significantly reduced the uptake efficiency of Fs and VFs by tumor cells in the lower chamber to 50.3% and 51.7%, respectively. In comparison, cRGD-VFs displayed much better ability to target Hepa1-6 tumor cells than other treatments, even under the interception of normal liver cells. Flow cytometry analysis confirmed the lower capture of cRGD-VFs in AML12 normal cells compared with Fs and VFs, while the relative uptake efficiency of tumor cells was enhanced to 62% (Figure 2e). Together, these results confirmed that the modification of cRGD on the ferritin-based vector was beneficial to improve the tumor-specific targeting. Then, the lysosomal escape ability of cRGD-VFs was further investigated. As shown in Figure S9 (Supporting Information), cRGD-VFs labeled with Cy5 (red fluorescence) was clearly co-localized with the green fluorescent lysosomes after 1 h of co-incubation with tumor cells. After 2 h, the overlap of cRGD-VFs with lysosomes decreased. When the co-incubation time was further extended to 4 h, significantly reduced co-localization was observed compared to that at 1 and 2 h, indicating the successful lysosomal escape of cRGD-VFs.

Subsequently, the cytotoxicity of different formulations towards liver tumor cells was carried out through CCK8 assay (Figure 2f). Specifically, Fn and VF exhibited negligible cytotoxicity within the setting concentration. By contrast, the cell viability of VFs-treated cells dropped down to 50.4%, while cRGD-VFs further led to a lower cell viability of 22.7% at the same concentration, which could be attributed to the enhanced tumor-specific endocytosis. Moreover, no obvious effects on cell viability of 3T3 normal cells and AML12 liver cells were observed in different formulations (Figures S10 and S11, Supporting Information). This could be in consequence of the relatively fewer endocytosis of cRGD-VFs by normal cells with a lower expression of RGD receptor (Figure S12, Supporting Information). Then, the mechanism of cRGD-VFs-mediated mitochondria dysfunction in tumor cells was carefully investigated (Figure 2g). As designed, cRGD-VFs would recruit E3 ligase under the influence of VHL ligands and eventually induce the proteolysis of ferritin to release iron ion, resulting in the rise of intracellular Fe^{2+} level and the release of siRNA. As shown in Figure S13 (Supporting Information), the brighter red fluorescence of FerroOrange was evidently observed in VF, VFs, and cRGD-VFs-treated cells, which witnessed the increase of intracellular Fe^{2+} level than other treatments, reflecting the degradation of ferritin shell. With the self-triggering proteolysis of the ferritin shell, the released siRNA would initiate ENO1-targeted regulation. As shown in Figure 2h,i, the down-regulation of ENO1 mRNA and the increased IRP1 mRNA in the Hepa1-6 tumor cells were found following cRGD-VFs-mediated ENO1 knockdown via quantitative polymerase chain reaction (qPCR) detection. Moreover, western blotting (WB) analysis revealed the dramatically decreased expression of ENO1 and the increased expression of IRP1 and Mfrn1 in the Hepa1-6 tumor cells treated with cRGD-VFs (Figure 2j), indicating the robust ability of cRGD-VFs to regulate the ENO1-IRP1-Mfrn1 axis. It should be noted that Mfrn1 serves as a mitochondrial iron homeostasis moderator by transporting Fe^{2+} from the cytoplasm to the mitochondria. As the direct evidence of mitochondrial iron overload, mitochondrial Fe^{2+} (mito-Fe^{2+}) was examined using the Mito-Ferro Green probe. As shown in Figure 2k, the markedly increased green fluorescence of mito-Fe^{2+} was detected in the Hepa1-6 tumor cells treated with cRGD-VFs, which was significantly stronger than the other groups, and further quantified by flow cytometric analysis (Figure 2l). These results could be the composite effects of the upregulation of mitochondrial iron channels following ENO1-IRP1-Mfrn1 axis regulation and Fe^{2+} self-provision from the proteolysis of ferritin. Excessive mitochondrial iron can mediate the production of mitochondrial ROS (mito-ROS), which was then detected by MitoSOX-Red staining (Figure 2m). The strongest red fluorescence signal of mito-ROS was caught in cRGD-VFs-treated tumor cells (Figure 2n), which was 2.0-fold, 2.0-fold, 2.2-fold, 1.4-fold, and 1.2-fold of that in control, Fn, VF, Fs, and VFs group, respectively (Figure S14, Supporting Information). Furthermore, as demonstrated by JC-1 staining, the significantly attenuated red fluorescence and the intensive green fluorescence were observed in tumor cells treated with cRGD-VFs (Figure 2o). Flow cytometric analysis quantified the significant decrease of mitochondrial membrane potential (MMP) after cRGD-VFs treatment, revealing the severe damage of mitochondrial membrane (Figure 2p). Taken together, these results illustrated that cRGD-VFs could produce excessive toxic mito-ROS by inducing mito-Fe^{2+} overload, which caused direct damages of mitochondrial membrane to subsequently trigger mitochondrial dysfunction.

Furthermore, Mito-Tracker Red was used to evaluate mitochondrial activity. As shown in Figure 2q, elongated mitochondria with strong red fluorescence were observed in control tumor cells. Similar mitochondrial morphology was also found in Fn-treated and VF-treated tumor cells, indicating the intact morphology and maintained activity of the mitochondria. In contrast, Fs treatment led to shortened mitochondria, and just punctate red fluorescence could be observed, suggesting the occurrence of

without the interception by AML12 liver cells. f) Cell viability of Hepa1-6 tumor cells after incubation with various formulations at different concentration. g) Schematic illustration of cRGD-VFs-triggered mitochondrial dysfunction. Relative mRNA level of h) ENO1 and i) IRP1 in Hepa1-6 tumor cells after various treatments. j) Evaluation of ENO1, IRP1 and Mfrn1 expression in Hepa1-6 tumor cells after various treatments by western blotting. k) CLSM images of mitochondrial Fe^{2+} stained with Mito-Ferro Green after various treatments. Scale bar: 20 µm. l) Flow cytometric analysis of mitochondrial Fe^{2+}. m) CLSM images of mitochondrial ROS stained with MitoSOX Red after various treatments. Scale bar: 50 µm. n) Flow cytometric analysis of mitochondria ROS. o) CLSM images of mitochondrial membrane potential stained by JC-1 after various treatments. Scale bar: 20 µm. p) Flow cytometric analysis of JC-1. q) CLSM images of Mito-Tracker Red-stained mitochondria in Hepa1-6 tumor cells with different treatments. Scale bar: 20 µm. r) Detection of mitochondrial morphology of Hepa1-6 tumor cells after various treatments by Bio-TEM. Data were presented as mean values ± SD. *n* = 3 biologically independent samples in Figure c–e,h,i. *n* = 5 biologically independent samples in Figure f. Images in Figure a,k,m,o,q,r were representative data from one independent experiment in each group. Statistical significance was calculated by one-way ANOVA with Tukey's multiple comparisons test.

© 2025 Wiley-VCH GmbH

15214095, 0, Downloaded from https://advanced.onlinelibrary.wiley.com/doi/10.1002/adma.202508457 by University Of British Columbia, Wiley Online Library on [01/09/2025]. See the Terms and Conditions (https://onlinelibrary.wiley.com/terms-and-conditions) on Wiley Online Library for rules of use; OA articles are governed by the applicable Creative Commons License

mitochondrial damage. Among all treatments, cRGD-VFs treatment resulted in the most severe mitochondrial destruction. The loss of filamentous morphology of mitochondria was evidently found in cRGD-VFs-treated tumor cells, accompanied by the markedly attenuated red fluorescence, which demonstrated a decline in mitochondrial activity. Moreover, biological TEM (Bio-TEM) was used to directly observe the damage of mitochondria after different treatments (Figure 2r). Compared with normal mitochondria in the control group, cRGD-VFs treatment contributed to the obvious structural damage of mitochondria in tumor cells, typically characterized by ridge fracture and membrane rupture, and a decrease in number. Collectively, it was demonstrated that cRGD-VFs-mediated mitochondrial iron metabolism perturbation would lead to mitochondrial dysfunction, which was lethal to tumor cells.

2.4. cRGD-VFs Triggered Immunogenic Tumor Cell Death to Activate the Antitumor Immune Cycle

Mitochondrial damage would accelerate the occurrence of tumor cell death. Mechanistically, cRGD-VFs-mediated mitochondrial oxidative stress led to mitochondrial dysfunction, which would further destroy intracellular redox homeostasis to induce tumor cell death. As shown in **Figure 3**a, intense ROS generation in cRGD-VFs-treated tumor cells was confirmed by the dramatically strong green fluorescence of DCFH-DA, which was significantly more than in other treated groups, and these results were further quantified by flow cytometric analysis (Figure 3b,c). As a consequence of iron overload-related oxidative stress, cRGD-VFs may elicit lipid peroxidation (LPO). Therefore, C11-BODIPY 581/591 was selected as a probe to evaluate the LPO level in tumor cells after various treatments. As shown in Figure S15 (Supporting Information), strong red fluorescence of non-oxidized lipids and faint green fluorescence of oxidized lipids were observed in the control tumor cells. By contrast, VFs-treated tumor cells exhibited significantly enhanced green fluorescence along with weakened red fluorescence, suggesting the occurrence of LPO. In all the treatment groups, cRGD-VFs induced the most severe LPO, as evidenced by the strongest green fluorescence from oxidized lipids, indicating that cRGD-VFs would induce ferroptotic tumor death.

Moreover, flow cytometric analysis showed that cRGD-VFs treatment induced severe tumor cell death with an apoptosis rate of 70.6% because of the severely disturbed mitochondrial iron homeostasis (Figure 3d), which was prominently higher than that of Control (6.2%), Fn (8.5%), VF (8.8%), Fs (26.1%), and VFs (48.0%), respectively. As a typical result of mitochondrial dysfunction, the lowest intracellular ATP level in cRGD-VFs-treated tumor cells was observably found (Figure 3e), indicating the insufficient energy supply for cellular activity. The dying tumor cells would release tumor-associated antigens and damage-associated molecular patterns (DAMPs). As an example, when tumor cell death occurred, the high mobility group box 1 (HMGB1) would migrate from the cell nucleus to the cytoplasm, and eventually be released into the extracellular space.[41,42] Noteworthily, the highest HMGB1 release was detected in the tumor cells treated with cRGD-VFs (Figure 3f,g). Moreover, the most pronounced calreticulin (CRT) expression was found on the surface of cRGD-VFs-treated tumor cells, which was witnessed by immunofluorescence staining (Figure 3h). Quantitative analysis from flow cytometry determined that the population of CRT positive tumor cells grew from ≈5.0% in the control group to 30.7% with the treatment of cRGD-VFs (Figure 3i,j). To sum up, these results fully demonstrated that cRGD-VFs-mediated mitochondrial iron overload could effectively induce the immunogenic cell death of tumor cells.

The release of DAMPs played a vital role in kick-starting the cancer-immunity cycle by stimulating the activation of antigen-presenting cells (APCs) (Figure 3k). As for adaptive immunity, bone marrow-derived dendritic cells (BMDCs) were incubated with the tumor cell supernatant with different treatments. Then, the maturation of treated BMDCs was investigated through detecting the expression of costimulatory molecules CD80 and CD86. As shown in Figure 3l and Figure S16 (Supporting Information), the most pronounced upregulation of CD80 and CD86 on BMDCs was detected in cRGD-VFs group, testifying that the ample DAMPs released from tumor cells accelerated the maturation of BMDCs. Matured BMDCs would further initiate T cell activation. As analyzed by flow cytometry, splenic T cells after co-incubating with different stimulated BMDCs displayed varying degrees of activation (Figure 3m). Among all the treatments, cRGD-VFs induced the most dramatic activation of T cells (30.5%), which was significantly higher than the control (11.1%), Fn (13.1%), VF (13.6%), Fs (21.3%), and VFs (27.2%) (Figure S17, Supporting Information), respectively. The activated T cells displayed powerful tumor killing ability, as more than 80% tumor cell death was specifically triggered by the T cells under the stimulus of cRGD-VFs (Figure S18, Supporting Information). These results proved the superior ability of cRGD-VFs to activate antitumor adaptive immunity. Particularly, macrophages are the representative APCs in the innate immunity. Therefore, whether cRGD-VFs-treated tumor cells could enhance the phagocytosis of macrophages was next investigated. As shown in Figure 3n, the green fluorescence-labeled tumor cells (with the treatment of Fn, VF, Fs and VFs, respectively) escaped from the engulfment of macrophages, with the colocalization of green and red fluorescence was rarely observed. In contrast, cRGD-VFs-treated tumor cells successfully awakened the phagocytosis of macrophages, as green fluorescence-labeled tumor cells were encompassed with red fluorescence-labeled macrophages. Flow cytometric analysis demonstrated the phagocytosis rate of macrophages cocultured with cRGD-VFs-treated tumor cells (27.7%) was ≈4.7-fold higher than that of the control group (4.9%) (Figure S19, Supporting Information). Taken together, these results indicated that cRGD-VFs-mediated mitochondrial iron overload would evoke the immunogenic death of tumor cells to release DAMPs and subsequently trigger the antitumor immunity cycle.

In addition, the inhibitory effect of cRGD-VFs on the migration and invasion of tumor cells was evaluated. As depicted in Figure S20 (Supporting Information), cRGD-VFs treatment significantly undermined the migration capacity of tumor cells as evidenced by the drastically decreased number of tumor cells crossing the transwell. A similar phenomenon was also observed in the invasion assay (Figure S21, Supporting Information). These results showed the positive effects of cRGD-VFs on the inhibition of tumor expansion and metastasis.

© 2025 Wiley-VCH GmbH

15214095, 0, Downloaded from https://advanced.onlinelibrary.wiley.com/doi/10.1002/adma.202508457 by University Of British Columbia, Wiley Online Library on [01/09/2025]. See the Terms and Conditions (https://onlinelibrary.wiley.com/terms-and-conditions) on Wiley Online Library for rules of use; OA articles are governed by the applicable Creative Commons License

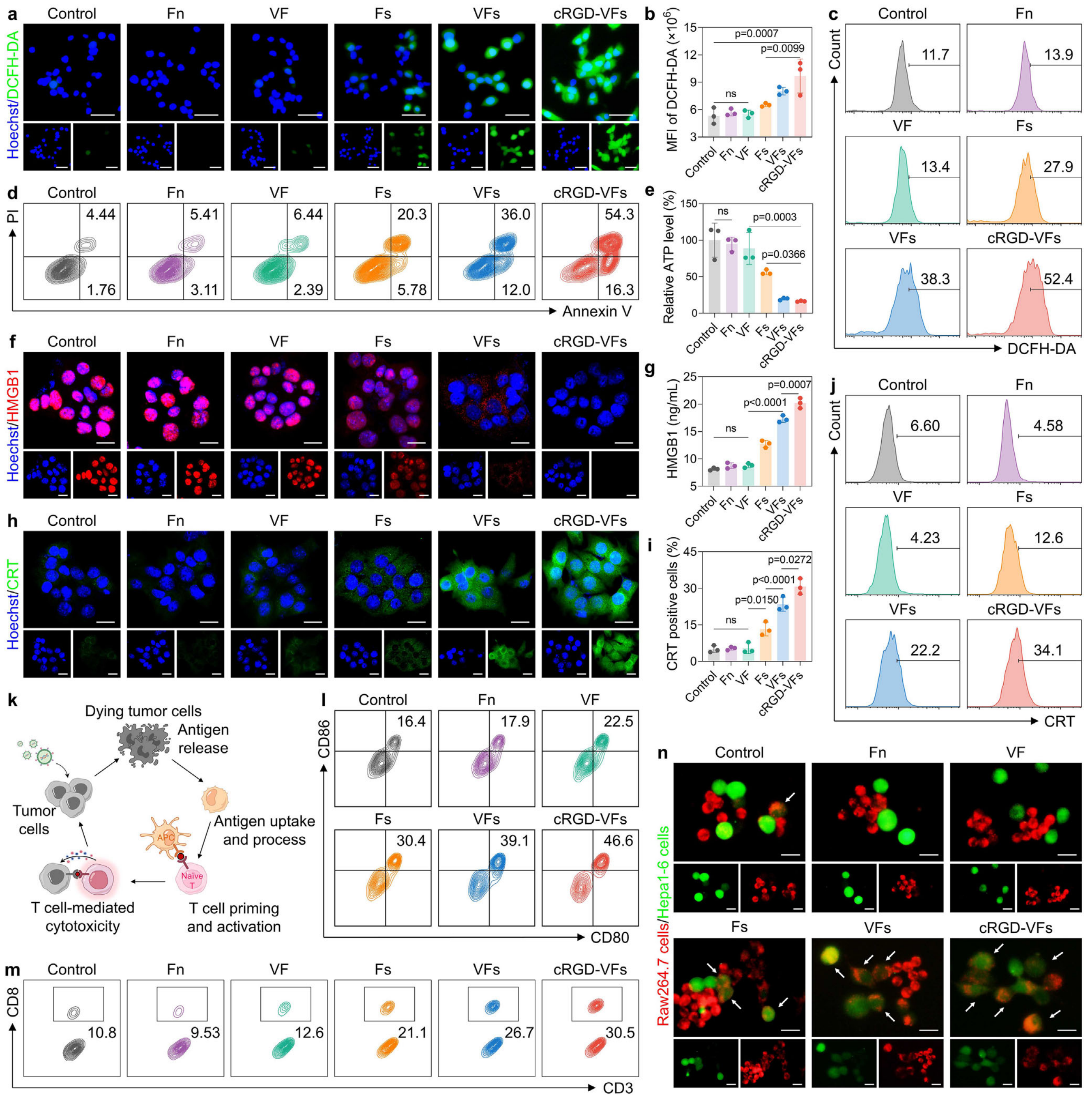

Figure 3. Evaluation of cRGD-VFs-mediated immunogenic tumor cell death and immune activation. a) CLSM images of intracellular ROS generation after various treatments. Scale bar: 50 µm. b) MFI of DCFH-DA signal and c) the representative flow cytometric analysis. d) Flow cytometric analysis of apoptotic tumor cells after various treatments. e) Relative intracellular ATP level after various treatments. f) Immunofluorescence staining of HMGB1 in tumor cells after various treatments. Scale bar: 20 µm. g) Extracellular HMGB1 content after various treatments. h) Immunofluorescence staining of CRT exposure on tumor cells after various treatments. Scale bar: 20 µm. i) Quantitative results of CRT-positive tumor cells and j) the representative flow cytometric analysis. k) Schematic illustration of the cancer-immunity cycle evoked by cRGD-VFs. l) Flow cytometric analysis of matured BMDCs ($CD11c^+CD80^+CD86^+$) after cocultured with differently treated tumor cells. m) Flow cytometric analysis of activated T cells ($CD3^+CD8^+$) after cocultured with differently treated BMDCs. n) CLSM images of the phagocytosis of differently treated tumor cells by macrophages. Scale bar: 20 µm. Data were presented as mean values ± SD. *n* = 3 biologically independent samples in Figure b,e,g,i. Images in Figure a,f,h,n were representative data from one independent experiment in each group. Statistical significance was calculated by one-way ANOVA with Tukey's multiple comparisons test.

© 2025 Wiley-VCH GmbH

15214095, 0, Downloaded from https://advanced.onlinelibrary.wiley.com/doi/10.1002/adma.202508457 by University Of British Columbia, Wiley Online Library on [01/09/2025]. See the Terms and Conditions (https://onlinelibrary.wiley.com/terms-and-conditions) on Wiley Online Library for rules of use; OA articles are governed by the applicable Creative Commons License

2.5. Evaluation of cRGD-VFs-Mediated Therapeutic Effects in Subcutaneous Liver Tumor Model

For in vivo study, the tumor-targeting ability of ferritin-based vectors was first investigated. As shown in **Figure 4a**, Fs, VFs, and cRGD-VFs arrived at tumor sites within 2 h after intravenous injection as determined by in vivo imaging system (IVIS). Then, a distinct fluorescence signal was detected at the tumor sites in cRGD-VFs-administered mice, which was significantly stronger than that of Fs-treated and VFs-treated ones, indicating the modification of tumor-targeting cRGD peptides efficiently enhanced the intratumoral cumulation efficiency of the designed cRGD-VFs. Furthermore, images of excised tissues further revealed the distribution of various formulations in different organs and tumors (Figure 4b,c). It could be seen that Fs was mostly intercepted in livers since the fluorescence intensity of tumor tissues were much weaker than that of livers. By contrast, the fluorescence intensity of tumor tissues in the mice treated with cRGD-VFs was significantly stronger, while comparatively weaker fluorescence was observed in livers. These results demonstrated the efficient tumor targeting and accumulation of cRGD-VFs, laying a solid foundation for effective cancer treatment.

Moreover, the therapeutic effects of cRGD-VFs were evaluated in the subcutaneous tumor model of mouse liver cancer (Figure 4d). As compared to the control group, VF treatment only had a little effect on tumor inhibition (Figure 4e,g), and Fs treatment could retard tumor growth to a certain degree but failed to produce inhibitory effects. Although VFs treatment led to a decrease in tumor volume during the therapeutic course, the growth of tumors rebounded after therapy discontinuance. Worth noting, cRGD-VFs treatment significantly inhibited tumor progression as evidenced by the flat tumor growth curve, and succeeded in controlling tumors to a relatively smaller volume. Moreover, cRGD-VFs treatment achieved a remarkable effect in prolonging the survival time of tumor-bearing mice (Figure 4f). For an in-depth understanding of the antitumor effects of cRGD-VFs, tumor tissues were collected for pathological analysis. As evidenced by hematoxylin-eosin (H&E) staining, cRGD-VFs induced the most severe damage of tumor tissues (Figure 4h). In addition, the expression of Ki67, a typical marker of cell proliferation, in the tumors treated with cRGD-VFs was found to be relatively lower than in other groups, proving the significant tumor inhibitory effect of cRGD-VFs (Figure 4i). Moreover, the rather weak fluorescence signal of ROS was detected in the control and VF group (Figure 4j). By comparison, the intensive ROS signal in cRGD-VFs-treated tumors revealed the disturbance of intratumoral redox homeostasis, thereby producing direct toxic effects on tumor cell growth.

To be noted, no abnormal fluctuation of body weights was observed in all treated mice (Figure S22, Supporting Information), along with that no obvious damages were found in H&E staining of major organs (Figure S23, Supporting Information), indicating the minimal systemic toxicity of cRGD-VFs treatment. Additionally, blood analyses exhibited no significant difference among different treatments in blood biochemical indexes and blood routine indexes (Figures S24 and S25, Supporting Information). These results collectively demonstrated that the designed cRGD-VFs had the favorable biocompatibility for in vivo antitumor application.

2.6. cRGD-VFs Evoked the Antitumor Immunity Through the Proactive Regulation of Immune-Related Pathways

Then, the in vivo immunological changes mediated by the engineered cRGD-VFs were further examined. Firstly, the intratumoral expression of immunostimulatory molecules was evaluated (Figure S26, Supporting Information). The immunological staining of tumor tissues revealed that the most pronounced exposure of CRT and the lowest level of HMGB1 after cRGD-VFs treatment, demonstrating that cRGD-VFs could effectively elicit tumor immunogenic cell death. Thereafter, tumor draining lymph nodes (TDLNs) were collected for DCs analysis. As shown in **Figure 5a**, the population of matured DCs ($CD80^+CD86^+$ in $CD11c^+$ cells) in cRGD-VFs group was 36.0%, which was 3.5-fold, 2.8-fold, 1.8-fold, and 1.2-fold of that in the control, VF, Fs, and VFs group, respectively. Moreover, cRGD-VFs treatment pronouncedly enhanced the intratumoral infiltration of T cells ($CD4^+/CD8^+$ in $CD3^+$ cells) (Figure 5b,c), especially for the activated effector $CD8^+$ T cells. Flow cytometry analysis determined the nearly triple increase in the frequency of $CD8^+$ T cells in cRGD-VFs group (48.3%) as compared with the control group (12.5%), reifying the robust antitumor adaptive immunity activated by cRGD-VFs. In addition, the enhanced recruitment of antineoplastic M1 macrophages ($F4/80^+CD86^+$ in $CD11b^+$ cells) was evidently found in the tumors with cRGD-VFs treatment (Figure 5d), substantiating the activation of innate immunity. It was also verified that cRGD-VFs facilitated the differentiation of memory T cells in the spleen as evidenced by the highest levels of central memory T cells (T_{CM}, $CD44^+CD62L^+$ in $CD8a^+$ cells, 9.14%) and effector memory T cells (T_{EM}, $CD44^+CD62L^-$ in $CD8a^+$ cells, 10.4%) among all treatments (Figure 5e–g), demonstrating the promising potential of cRGD-VFs for building antitumor immunologic memory.

To evaluate cRGD-VFs-mediated immune activation, transcriptomics analyses were applied to explicitly investigate the immunotherapeutic mechanisms of cRGD-VFs. Principal component analysis (PCA) exhibited the separation between the control group and cRGD-VFs group, manifesting that cRGD-VFs induced significant transcriptomic alterations of tumor tissues (Figure 5h). Concretely, 324 upregulated genes and 122 downregulated genes were distinguished from the control group after cRGD-VFs treatment (p value<0.05, fold changes≥ 2) (Figure 5i,j). We surprisingly found that these differentially expressed genes were mainly concentrated in immune-related pathways (Figure 5k), such as immune system process and immune response from gene ontology (GO) enrichment. Kyoto Encyclopedia of Genes and Genomes (KEGG) pathway analysis showed the significant changes in T cell-associated pathways (Figure 5l), including Th1 and Th2 cell differentiation, Th17 cell differentiation, and T cell receptor signaling pathway. Specifically, cluster analysis of differentially expressed genes showed the upregulation of genes associated with immune response regulation (e.g., Cd4, Cd3g, Ifng, Cd3e), and genes closely related to T cell activation (e.g., Cxcr3, Cd28, Tnfsf9, Gzmf, Cxcr6) were also found upregulated (Figure 5m). In addition, as shown in Figure 5n–p, the gene set enrichment analysis (GSEA) revealed the positive involvement of T cell activation, cytokine-cytokine receptor interaction, and immune system process in cRGD-VFs-mediated immune activation. Together, these results

© 2025 Wiley-VCH GmbH

15214095, 0, Downloaded from https://advanced.onlinelibrary.wiley.com/doi/10.1002/adma.202508457 by University Of British Columbia, Wiley Online Library on [01/09/2025]. See the Terms and Conditions (https://onlinelibrary.wiley.com/terms-and-conditions) on Wiley Online Library for rules of use; OA articles are governed by the applicable Creative Commons License

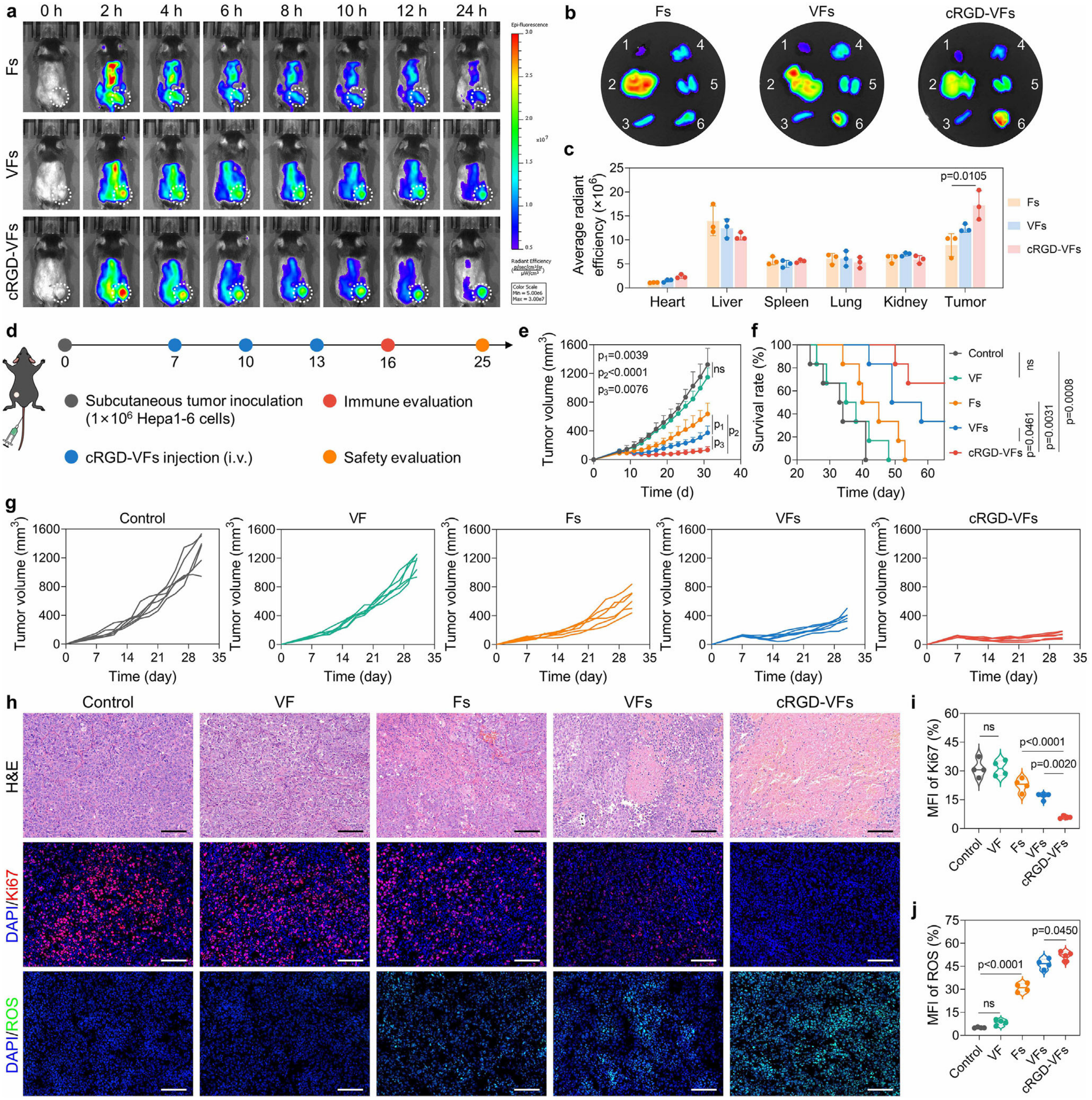

Figure 4. Study of in vivo bio-distribution and antitumor effects of cRGD-VFs. a) In vivo fluorescence imaging of Hepa1-6 tumor-bearing mice intravenously injected with Cy5-labelled Fs, VFs, and cRGD-VFs, respectively. b) Ex vivo fluorescence images of the main organs and tumors, and c) the corresponding quantitative average radiant efficiency. (1: Heart, 2: Liver, 3: Spleen, 4: Lung, 5: Kidney, 6: Tumor) d) Schematic illustration of the treatment schedule for Hepa1-6 tumor-bearing mice. e) Average tumor growth curves and f) survival curves of tumor-bearing mice after various treatments. g) Individual tumor growth curves. h) H&E staining, Ki67 staining, and ROS staining of tumor tissues with different treatments. Scale bar: 50 µm. i) Quantitative results of intratumoral Ki67 expression analyzed by Image J. j) Quantitative results of intratumoral ROS level analyzed by Image J. Data were represented as mean values ± SD. *n* = 3 biologically independent mice in Figure c. *n* = 6 biologically independent mice in Figure e–g. Images in Figure h were representative data from one of four independent mice in each group. *n* = 4 in Figure i,j from three biologically independent mice tumor tissue images. Statistical significance was calculated by one-way ANOVA with Tukey's multiple comparisons test.

© 2025 Wiley-VCH GmbH

15214095, 0, Downloaded from https://advanced.onlinelibrary.wiley.com/doi/10.1002/adma.202508457 by University Of British Columbia, Wiley Online Library on [01/09/2025]. See the Terms and Conditions (https://onlinelibrary.wiley.com/terms-and-conditions) on Wiley Online Library for rules of use; OA articles are governed by the applicable Creative Commons License

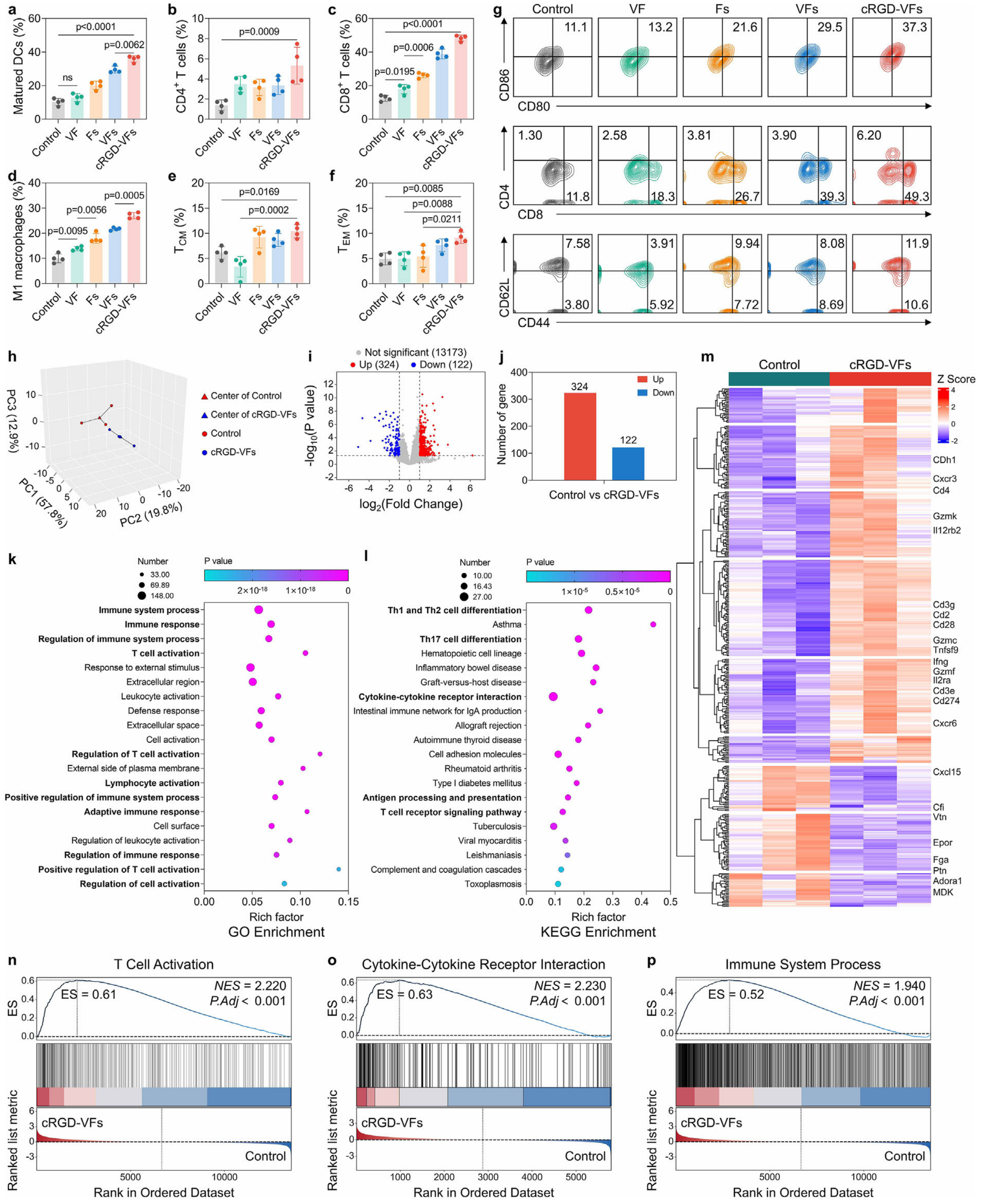

Figure 5. Evaluation of cRGD-VFs-mediated the antitumor immunity by transcriptomic analysis. a) Quantification of matured DCs in tumor-draining lymph nodes. Quantification of tumor-infiltrating b) $CD4^+$ T cells, c) $CD8^+$ T cells, and d) M1 macrophages. Quantification of e) T_{CM} and f) T_{EM} in spleens. g) Representative flow cytometric analysis of DCs, intratumoral T cells and splenic memory T cells. h) Principal component analysis (PCA) of tumor samples (*n* = 3). i) Volcano plot of differentially expressed genes after cRGD-VFs treatment and j) the corresponding histogram. Analysis of the main pathways in which the differentially expressed genes were enriched after cRGD-VFs treatments by k) GO enrichment and l) KEGG enrichment. m) Heatmap for identification of the differentially expressed genes in tumor tissues after cRGD-VFs treatment. GSEA enrichment analysis for the representative upregulated pathway of n) T cell activation, o) cytokine-cytokine receptor interaction, and p) immune system process. Data were represented as mean values ± SD. *n* = 4 biologically independent mice in Figure a–f. *n* = 3 biologically independent mice in Figure h–p. Statistical significance was calculated by one-way ANOVA with Tukey's multiple comparisons test in Figure a–f.

15214095, 0, Downloaded from https://onlinelibrary.wiley.com/doi/10.1002/adma.202508457 by University Of British Columbia, Wiley Online Library on [01/09/2025]. See the Terms and Conditions (https://onlinelibrary.wiley.com/terms-and-conditions) on Wiley Online Library for rules of use; OA articles are governed by the applicable Creative Commons License

15214095, 0, Downloaded from https://advanced.onlinelibrary.wiley.com/doi/10.1002/adma.202508457 by University Of British Columbia, Wiley Online Library on [01/09/2025]. See the Terms and Conditions (https://onlinelibrary.wiley.com/terms-and-conditions) on Wiley Online Library for rules of use; OA articles are governed by the applicable Creative Commons License

demonstrated that cRGD-VFs treatment broadly activated antitumor immune responses, especially for T cell-mediated immunity against tumors.

2.7. The synergy of cRGD-VFs and PD-L1 Blockade Succeeded in the Eradication of Subcutaneous and Rechallenged Tumors

Although the therapeutic effects of cRGD-VFs had been carried out in the subcutaneous liver tumor model, the transcriptome analysis revealed the unexpected upregulation of PD-L1 (Cd274) after cRGD-VFs therapy (Figure 5m), which may promote immune evasion of the tumor through PD-L1/PD-1 axis to elude the hunting from immune cells activated by cRGD-VFs. Thus, it was reasonably conjectured that the synergy of cRGD-VFs and immune checkpoint blockade (ICB) could achieve a superior therapeutic outcome. On this basis, the subcutaneous hepatic tumor model was established, and tumor-bearing mice received PD-1 antibody (αPD-1) injection after 24 h of cRGD-VFs administration (**Figure** 6a). As shown in Figure 6b,d, the combination of cRGD-VFs and αPD-1 exhibited a striking inhibition on tumor growth, as evidenced by the complete tumor eradication observed in two-thirds of the tumor-bearing mice after synergistic treatment (cRGD-VFs+αPD-1), while the tumor volume of the rest was controlled under 150 mm^3. Moreover, the survival lifetime of tumor-bearing mice treated with cRGD-VFs+αPD-1 was significantly extended with no death occurring during the whole therapeutic period (Figure 6c). H&E staining revealed the maximal damage in tumor tissues, while immunofluorescence staining showed the lowest expression of Ki67 symbolizing the minimal proliferative activity of tumor cells after the combination treatment (Figure 6e,f, and Figure S27, Supporting Information). Furthermore, the antitumor immune effects induced by the synergistic therapy were studied in depth to understand the cooperative effects of cRGD-VFs and αPD-1. As shown in Figure 6g, αPD-1-based monotherapy failed to improve DCs maturation and further enhance T cell activation. Contrastively, cRGD-VFs+αPD-1 stimulated a pronounced DCs maturation with the population of mature DCs enlarging from 12.4% in αPD-1 group to 32.3%, which was beneficial to activate effector T cells. Specifically, the level of intratumoral infiltration of CD4$^+$/CD8$^+$ T cells in the tumor tissues treated with cRGD-VFs+αPD-1 was 14.8%/26.1% (Figure 6h,i), which was significantly higher than that of the control (10.7%/4.4%), αPD-1 (9.0%/4.9%), and cRGD-VFs (12%/17.6%) groups, respectively. These results were consistent with the directly visualized observation of CD4$^+$ and CD8$^+$ T cells in tumor tissues by immunofluorescence staining (Figure 6j). The strong activation of effector T cells could be ascribed to cRGD-VFs-mediated immune activation and the enhanced immunocompetence of cytotoxic T lymphocytes after PD-1 blockade. The systemic antitumor effects were further confirmed by the increased secretion of TNF-α (Figure S28a, Supporting Information), IFN-γ (Figure S28b, Supporting Information) and IL-12p70 (Figure S28c, Supporting Information) in the serum of cRGD-VFs+αPD-1-treated mice, as well as the relatively lower level of IL-10 was evidently detected in the cRGD-VFs+αPD-1-treated mice (Figure S28d, Supporting Information), indicating the alleviation of immune suppression. In addition, splenic memory T cells were also analyzed, and the remarkably increased population of T_{CM} and T_{EM} in the mice treated with cRGD-VFs+αPD-1 confirmed the robust antitumor immune memory effects (Figure 6k–m).

Motivated by the superior therapeutic outcomes and the favorable immune memory effects, the long-lasting antitumor effects were further studied. After 60 days for the first tumor inoculation, the surviving mice in cRGD-VFs+αPD-1 group were rechallenged with Hepa1-6 tumor cells on the other flank (Figure 6n). Mice of the same week-age with no history of tumor inoculation were selected as the control (Control) and inoculated with the same amount of tumor cells. As shown in Figure 6o–q, the rapid tumor growth was observed in the control group, while in stark contrast, the progression of rechallenged tumors was significantly inhibited in the cRGD-VFs+αPD-1 group, which was attributed to the systemic antitumor immunity and long-term immunological memory provoked by cRGD-VFs collaborated with αPD-1. As shown in Figure 6r–t, the frequency of circulating memory T cells (T_{CM}/T_{EM}) in the peripheral blood of mice treated with cRGD-VFs+αPD-1 (19.5%/22.8%) were much higher than that of the control group (15.3%/13.3%), indicating that the immune system awakened the defense mechanism based on immunological memory when perceiving the second threat from tumor cells. At the end of treatment, the spleens of mice from each group were collected for splenocyte analysis. As shown in Figure S29 (Supporting Information), a significantly higher proportion of CD4$^+$ and CD8$^+$ T cells was found in cRGD-VFs+αPD-1 group, manifesting the effectively activated antitumor immunity. What's more, the expanded T_{CM} and T_{EM} revealed the efficient building of immunologic memory after the synergistic treatment (Figure S30, Supporting Information). Moreover, as compared to the control, the increased secretion of TNF-α and IFN-γ in the mice serum after cRGD-VFs+αPD-1 treatment indicated the mobilization of systemic immune responses against tumor rechallenge (Figure S31, Supporting Information). Collectively, these results demonstrated that cRGD-VFs-mediated immune activation in combination with αPD-1 had superior antitumor effects and long-lasting immunological memory to treat the rechallenged tumors.

2.8. Evaluation of the Synergistic Therapeutic Effects of cRGD-VFs+αPD-1 Against Intractable Orthotopic Hepatocellular Carcinoma

Hepatocellular carcinoma has been likened to a silent killer due to the limited therapeutics, resulting in the stubbornly high mortality.[43] With this premise, an orthotopic hepatocellular carcinoma model was established to realistically evaluate the synergistic therapeutic effect of cRGD-VFs+αPD-1 (**Figure** 7a). In detail, in vivo imaging system (IVIS) was applied to monitor the growth progress of hepatocellular carcinoma. As shown in Figure 7b, the orthotopic hepatic tumors grew rapidly in the control group, as evidenced by the ever-increasing bioluminescence intensity of tumors. In addition, although the bioluminescence signals of tumors treated with single αPD-1 were slightly weaker, the dissatisfactory therapeutic outcomes reflected the limitation of mono ICB. Intriguingly, cRGD-VFs displayed a better therapeutic effect against orthotopic liver tumors than αPD-1. In stark contrast, the weakest bioluminescence intensity of tumors

© 2025 Wiley-VCH GmbH

15214095, 0, Downloaded from https://onlinelibrary.wiley.com/doi/10.1002/adma.202508457 by University Of British Columbia, Wiley Online Library on [01/09/2025]. See the Terms and Conditions (https://onlinelibrary.wiley.com/terms-and-conditions) on Wiley Online Library for rules of use; OA articles are governed by the applicable Creative Commons License

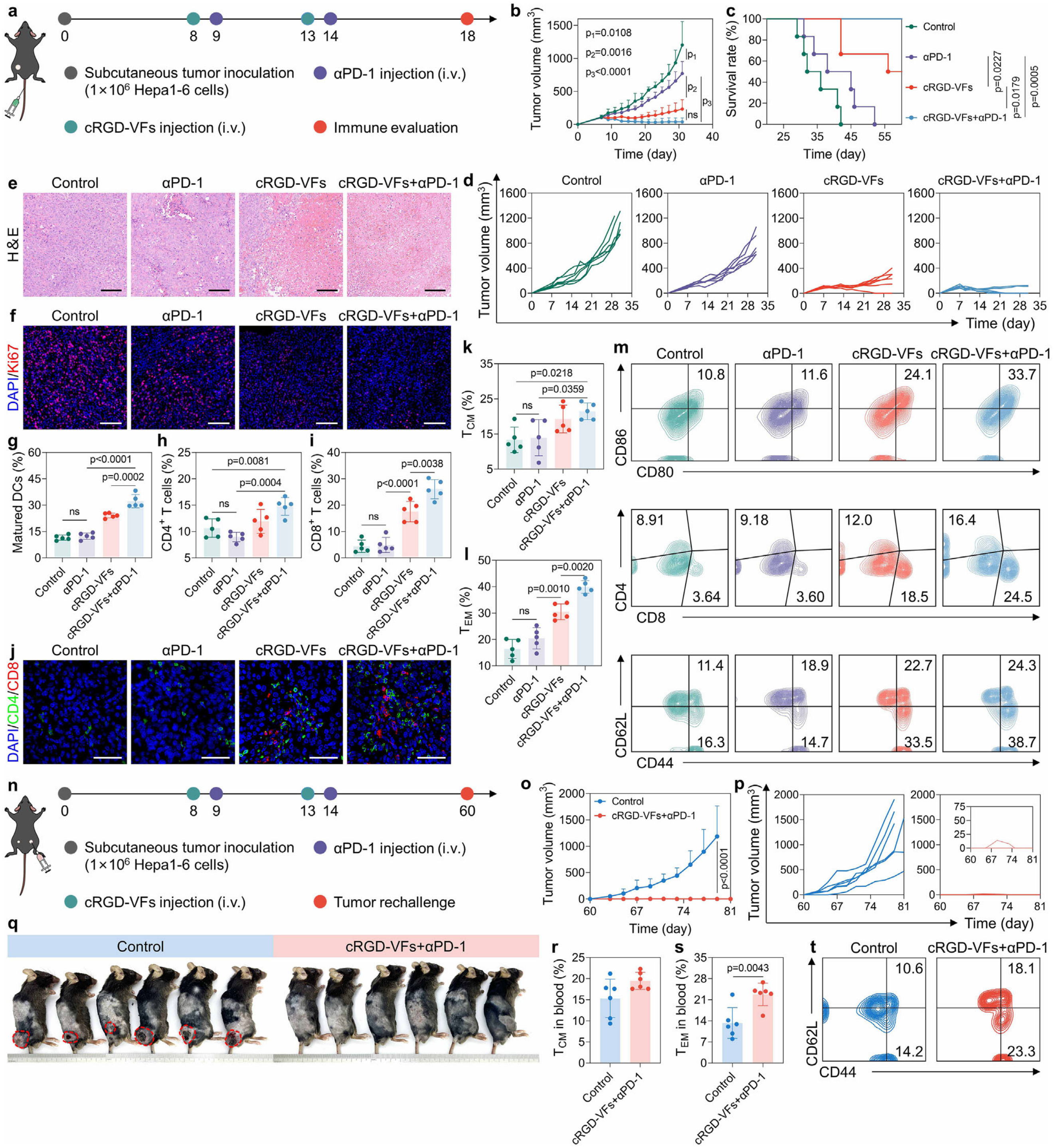

Figure 6. The synergistic effects of cRGD-VFs and PD-1 blockade in eliminating subcutaneous and rechallenged tumors. a) Schematic illustration of the synergistic treatment schedule for Hepa1-6 tumor-bearing mice. b) Average tumor growth curves and c) survival curves of tumor-bearing mice in different groups. d) Individual tumor growth curves. e) H&E and f) Ki67 staining of tumor tissues with different treatments. Quantitative results of g) matured DCs in TDLNs, h) intratumoral $CD4^+$ T cells, and i) $CD8^+$ T cells. j) Immunofluorescence staining of $CD4^+$ T cells and $CD8^+$ T cells in tumor tissues after various treatments. Quantitative results of k) T_{CM} and l) T_{EM} in spleens. m) Representative flow cytometric analysis of matured DCs, intratumoral T cells, and splenic memory T cells. n) Schematic illustration of the synergistic treatment schedule of Hepa1-6 rechallenged tumors. o) Average tumor growth curves and p) individual tumor growth curves of tumor-bearing mice. q) Photograph of mice on day 14 after tumor rechallenge. Quantitative results of r) T_{CM} and s) T_{EM} in mouse peripheral blood and t) the representative flow cytometric analysis. Data were represented as mean values ± SD. $n = 6$ biologically independent mice in Figure b-d. $n = 5$ biologically independent mice in Figure g–i,k,l. Images in Figure e,f,j were representative data from one of five independent mice in each group. $n = 6$ biologically independent mice in Figure o-s. Statistical significance was calculated by one-way ANOVA with Tukey's multiple comparisons test in Figure g-i,k,l. Statistical significance was calculated by an unpaired t-test in Figure s.

© 2025 Wiley-VCH GmbH

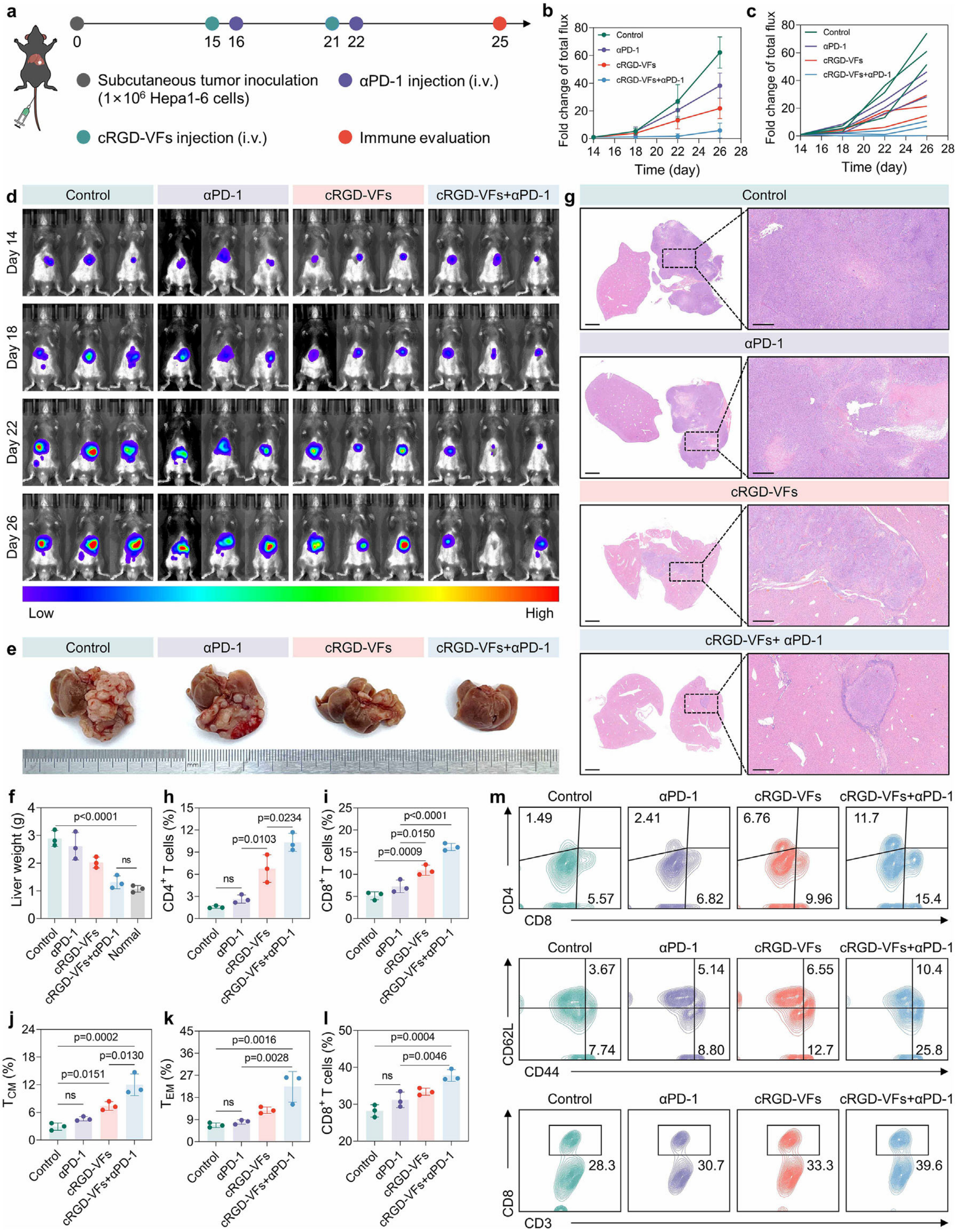

Figure 7. The synergistic therapeutic effects of cRGD-VFs and αPD-1 in intractable orthotopic hepatic carcinoma model. a) Schematic illustration of the synergistic treatment schedule for orthotopic hepatic tumor-bearing mice. b) Tumor growth curves analyzed from tumor bioluminescence intensity, and c) the individual tumor growth curves. d) Bioluminescence images of orthotopic liver tumor-bearing mice receiving different treatments at the indicated time points. e) Representative photograph of the livers of mice with different treatments. f) Liver weights of mice after different treatments. g) Representative H&E staining of the livers of mice after different treatments. The left panel displayed the pathological slices of the whole liver (Scale bar: 2000 µm), and the right panel displayed the partial enlarged views (Scale bar: 500 µm). Quantitative results of intratumoral h) $CD4^+$ T cells and i) $CD8^+$ T cells. Quantitative results of splenic j) T_{CM}, k) T_{EM}, and l) $CD8^+$ T cells. m) Representative flow cytometric analysis of immune cells. Data were represented as mean values ± SD. *n* = 3 biologically independent mice in Figure b–d, f, h–l. Images in Figure e,g were representative data from one of three independent mice in each group. Statistical significance was calculated by one-way ANOVA with Tukey's multiple comparisons test.

15214095, 0, Downloaded from https://advanced.onlinelibrary.wiley.com/doi/10.1002/adma.202508457 by University Of British Columbia, Wiley Online Library on [01/09/2025]. See the Terms and Conditions (https://onlinelibrary.wiley.com/terms-and-conditions) on Wiley Online Library for rules of use; OA articles are governed by the applicable Creative Commons License

© 2025 Wiley-VCH GmbH

was found in the cRGD-VFs+αPD-1 group, displaying the superior tumor remission (Figure 7c,d). Moreover, the representative photographs of excised livers intuitively displayed the tumor growth (Figure 7e). These results were consistent with the average weights of livers from orthotopic hepatocellular tumor-bearing mice after different treatments, laterally verifying the marked suppression of tumor growth in the combination group (Figure 7f). In addition, the H&E staining displayed the large cancerous region in the control and αPD-1 group, while tumors treated with cRGD-VFs were significantly shrank in volume (Figure 7g). Particularly, only a small tumor bulge could be observed in the livers of mice treated with cRGD-VFs+αPD-1, as demonstrated by the smallest lesion area discovered in H&E staining of liver tissues among all the treatments. Furthermore, immunological analysis revealed the most sufficient intratumoral infiltration of CD4$^+$ and CD8$^+$ T cells (Figure 7h,i) after cRGD-VFs+αPD-1 treatment (10.3% and 16.2%), which was prominently higher than that in the control group (1.6% and 5.2%), αPD-1 group (2.7% and 7.3%), and cRGD-VF group (6.8% and 10.9%), respectively. Moreover, the highest percentage of T$_{CM}$, T$_{EM,}$ and CD8$^+$ T cells was notably detected in the spleens of orthotopic hepatocellular tumor-bearing mice treated with cRGD-VFs+αPD-1 (Figure 7j–m), indicating the long-term protective immune memory effects of the synergistic therapy of cRGD-VFs+αPD-1. Taken together, these results comprehensively manifested the remarkable antitumor effects and robust immune activation of the combined therapy of cRGD-VFs and αPD-1, showing the promising potential to treat malignant tumors.

3. Conclusion

The abnormal iron homeostasis has been a promising target for tumor immunotherapy, yet the adaptive resistance of tumor cells towards iron disturbance remains a challenge for enhancing therapeutic efficacy. Thus, targeting the center of cellular iron metabolism and the specific acting site of inducing iron-related tumor death represents an emerging strategy. In this study, we notice the key role of ENO1-IRP1-Mfrn1 axis in regulating mitochondrial iron homeostasis, and present a proteolysis-triggered RNA interference system for ENO1-targeted knockdown to upregulate Mfrn1, therefore facilitating mitochondrial iron overload. Specifically, the engineered cRGD-VFs could trigger iron overload-related mitochondrial dysfunction via the comprehensive effects of ferritin proteolysis-based iron supply and RNA interference-mediated regulation of mitochondrial iron transport channels. Notably, cRGD-VFs-mediated mitochondrial iron overload effectively induces tumor cell death due to the severe mitochondrial destruction, and significantly activates antitumor immunity to eliminate tumors.

Regarding the translational potential, the engineered self-triggering proteolysis RNA interference system cRGD-VFs exhibits favorable biocompatibility due to the low immunogenicity of natural ferritin, which is advantageous for clinical application. The interference of the specific acting site ENO1 by cRGD-VFs shows highly effective tumor killing by the direct disturbance towards mitochondria, as evidenced by the remarkable tumor regression. Moreover, the synergy of cRGD-VFs and immune checkpoint blockade has demonstrated the superior immunological memory effects in the rechallenged tumor model, providing a potential strategy against tumor recurrence. Particularly, cRGD-VFs showed the marked tumor inhibition of intractable orthotopic hepatocellular carcinoma, which is promising to offer clinical benefits for liver cancer patients. In summary, our work provided an innovative strategy of regulating iron homeostasis at the suborganelle level for potentiating antitumor immunotherapy, highlighting new opportunities for high-performance cancer therapy.

4. Experimental Section

Materials: Ferritin (CAS: 9007-73-2) was purchased from Sigma–Aldrich. DBCO-NHS ester (CAS: 1353016-71-3) was purchased from Leyan, Shanghai, China. VH032-PEG2-N$_3$ (Cat#HY-103599) was purchased from MedChemExpress. cRGD-N$_3$ was synthesized by Nanjing Yuan-peptide Biotech Co., Ltd. ENO1 siRNA was designed and synthesized by GeneScript Corporation. Anti-ENO1 antibody (Cat#P08081) was purchased from ProMab Biotechnologies Inc. Anti-Mfrn1 antibody (Cat#BD-PN5334) was purchased from Biodragon. Anti-IRP1 antibody (Cat#ES6389) was purchased from ELK Biotechnology.

Cell Culture: Murine Hepa1-6 hepatoma cells and murine AML 12 liver cells were purchased from Pricella Life Science & Technology Co. Ltd. Hepa1-6/Luc cells were purchased from FuHeng Biology. Murine 3T3 embryonal fibroblasts and Raw264.7 macrophages were purchased from the China Center for Type Culture Collection (CCTCC). Cells were cultured at 37 °C with 5% CO$_2$ in culture medium supplemented with 10% (v/v) fetal bovine serum (VivaCell) and 1% penicillin-streptomycin (SP002030100, Sperikon Life Science & Biotechnology Co., Ltd.). Cell culture dish and cell culture plate were purchased from NEST Biotechnology Co., Ltd., Wuxi, China. Confocal dishes were purchased from SAINING Biotechnology.

Evaluation of Mitochondrial Damage: Specifically, Hepa1-6 tumor cells were seeded in 6-well plate ($\approx 2 \times 10^5$ cells per well) and incubated for 12 h. Then, Hepa1-6 tumor cells were treated with different nanoparticles. After incubation of 12 h, tumor cells were washed with PBS for three times. For mitochondrial membrane potential detection, tumor cells were stained with JC-1 and finally observed under a confocal microscope. For mitochondria activity detection, tumor cells were stained with Mito-Tracker Red (MitoScence Red CMXRos, Cat#M4067S, UElandy, Suzhou, China) and the cell nucleus was stained with Hoechst 33342, respectively. Stained cells were observed under a confocal microscope. For mitochondria morphology observation, the treated cells were collected and fixed with 2.5% glutaraldehyde for biological TEM observation.

Intracellular Oxidative Stress Detection: The generation of ROS in Hepa1-6 tumor cells was detected using DCFH-DA probes (Cat#AKCE002-1, Beijing Boxbio Science & Technology Co., Ltd.). Specifically, Hepa1-6 tumor cells were seeded in 6-well plate ($\approx 2 \times 10^5$ cells per well) and incubated for 12 h. Then, different formulations were added to each well and incubated with Hepa1-6 cells for 8 h. Afterwards, the culture medium was washed away using PBS. Subsequently, the treated cells were stained with DCFH-DA and Hoechst 33342, respectively. Stained cells were observed under a confocal microscope or collected for flow cytometry analysis.

Cell Apoptosis Assay: Hepa1-6 tumor cells were seeded in 12-well plates and incubated for 12 h. Then tumor cells were treated with different nanoparticles for further 24 h. Subsequently, the treated cells were collected and stained using Annexin V Alexa Fluor647/PI cell apoptosis detection kit (Cat#ZYFA001-0100, ZUNYAN, NanJing, China) according to the manufacturer's instruction. Stained cells were analyzed by flow cytometry.

Characterization of Immunogenic Tumor Cell Death In Vitro: Hepa1-6 tumor cells were seeded in 6-well plate ($\approx 2\times10^5$ cells per well) and incubated for 12 h. Then, different formulations were added to each well and incubated with Hepa1-6 cells for 12 h. The treated cells were collected for immunofluorescent staining to evaluate the release of HMGB1 and the exposure of CRT. Cell culture medium was collected for extracellular HMGB1 detection using a HMGB1 ELISA kit (Cat#EHRC01.48, Neobioscience Technology Co, Ltd.) according to the manufacturer's instructions.

© 2025 Wiley-VCH GmbH

15214095, 0, Downloaded from https://advanced.onlinelibrary.wiley.com/doi/10.1002/adma.202508457 by University Of British Columbia, Wiley Online Library on [01/09/2025]. See the Terms and Conditions (https://onlinelibrary.wiley.com/terms-and-conditions) on Wiley Online Library for rules of use; OA articles are governed by the applicable Creative Commons License

CRT expression was detected by flow cytometry after staining with Calreticulin Antibody: FITC (Cat#SPC-122B-FITC, Stress Marq). Intracellular ATP level was detected using an ATP assay kit (Cat#S0027, Beyotime).

Evaluation of cRGD-VFs-Mediated Immune Activation In Vitro: Specifically, bone marrow-derived dendritic cells (BMDCs) were obtained from C57BL/6 mice according to the mature protocol. Then, BMDCs were pretreated with 10 ng mL^{-1} IL-4 (Cat#PM1014, APExBIO, Houston, USA) and 20 ng mL^{-1} GM-CSF to induce the differentiation into immature DCs. Hepa1-6 tumor cells were pre-treated with different formulations for 24 h and the conditioned medium was collected. The prepared BMDCs were seeded in 6-well plates and incubated with the conditioned medium for 24 h. Then, the maturation of BMDCs was studied by flow cytometry.

Splenic T cells were obtained from C57BL/6 mice according to the mature protocol. Then, T cells were cocultured with BMDCs stimulated as mentioned above (BMDCs: T cells = 1:5). After 24 h, the cultured cells were collected and stained with FITC anti-mouse CD3 antibody (Cat#100204, Biolegend) and PE anti-mouse CD8a antibody (Cat#100708, Biolegend) for activated T cell detection by flow cytometry.

To determine the tumor specific killing of activated T cells, stimulated T cells were collected and further cocultured with Hepa1-6 tumor cells (T:Hepa1-6 ≈ 5:1) for 48 h. Then, suspending T cells were washed away and the cell viability of adherent tumor cells was detected by CCK8 assay.

Cell Migration and Invasion Assay: Specifically, Hepa1-6 tumor cells were seeded in 6-well plates (≈2×10^5 cells per well) and incubated for 12 h. Then, the cells were cocultured with different formulations for 12 h. Subsequently, differently treated tumor cells were collected and resuspended in serum-free medium, and then seeded on the upper chamber of a transwell insert (8 µm pore size) in 6-well plates. The lower chambers of 6-well plates were filled with serum-containing culture medium. After 24 h of incubation, the migrated/invaded cells were fixed 4% paraformaldehyde and stained with crystal violet. Then, the migrated/invaded cells were imaged under microscopy and counted by Image J. To be noted, the upper chamber of the transwell insert was coated with matrix gel (Cat#3D201-005, BaiDi Biotechnology Co., Ltd.) for the cell invasion assay before other experimental operations.

In Vivo Antitumor Effects: Hepa1-6 cell-derived subcutaneous tumor model was used to study the antitumor efficacy of cRGD-VFs. Specifically, Hepa1-6 cells (1×10^6 cells) were inoculated into the left flank of C57BL/6 mice. When the tumor volume reached ≈100 mm^3, mice were randomly divided into 5 groups ($n = 6$). Tumor-bearing mice were intravenously injected with different formulations: (1) PBS (Control), (2) VF, (3) Fs, (4) VFs, (5) cRGD-VFs on day 7, 10 and 13, respectively. Tumor volumes and body weight were measured every 2 days. At day 16, mice were sacrificed and tumors were collected for histological and immune analysis. The tumor tissues were homogenized for intratumoral cytokine evaluation. Mouse IFN-γ ELISA Kit (Cat#CME0003-096), Mouse IL-12p70 ELISA Kit (Cat#CME0013-F-096), and Mouse IL-10 ELISA Kit (Cat#CME0016-F-096) were purchased from 4A Biotech. Mouse TNF-α ELISA Kit (Cat#EK282) were purchased from Multisciences (LIANKE) Biotech Co., Ltd.

Circulating memory T Cells Analysis: Blood from tumor-bearing mice with various treatments were collected. Peripheral blood mononuclear cells (PBMCs) were isolated using an ELISA kit (Cat#P8620, Solarbio). Then the isolated PBMCs were stained with FITC anti-mouse CD8a antibody (Cat#100706, Biolegend), PE anti-mouse/human CD44 antibody (Cat#103008, Biolegend), and APC anti-mouse CD62L antibody (Cat#104412, Biolegend).

Statistical Analysis: Data are presented as mean ± SD, with the sample size (n) and error bar definitions specified in the figure legends. Group comparisons were performed using two-tailed Student's t-tests (for two groups) or one-way ANOVA followed by Tukey's post hoc test (for multiple groups). All analyses were conducted in GraphPad Prism 8.3.0 (GraphPad Software, CA, USA).

Supporting Information

Supporting Information is available from the Wiley Online Library or from the author.

Acknowledgements

S.-M.Z. and X.-K.J contributed equally to this work. This work was supported by the National Natural Science Foundation of China (52473145, 52333004, 52273301, 52131302, and 22135005), and Hubei Province Science and Technology Innovation Talent Program (2024DJA011).

Conflict of Interest

The authors declare no conflict of interest.

Data Availability Statement

The data that support the findings of this study are available from the corresponding author upon reasonable request.

Keywords

cancer immunotherapy, mitochondrial dysfunction, mitochondrial iron homeostasis, proteolysis, tumor-targeting

Received: May 4, 2025
Revised: July 16, 2025
Published online:

---

[1] X. Chen, R. Kang, G. Kroemer, D. Tang, *Nat. Rev. Clin. Oncol.* **2021**, *18*, 280.
[2] Q. Ru, Y. Li, L. Chen, Y. Wu, J. Min, F. Wang, *Signal Transduction Targeted Ther.* **2024**, *9*, 271.
[3] G. Lei, L. Zhuang, B. Gan, *Nat. Rev. Cancer* **2022**, *22*, 381.
[4] X. Jiang, B. R. Stockwell, M. Conrad, *Nat. Rev. Mol. Cell Biol.* **2021**, *22*, 266.
[5] Y. Zhou, S. Fan, L. Feng, X. Huang, X. Chen, *Adv. Mater.* **2021**, *33*, 2104223
[6] W. Xuan, Y. Xia, T. Li, L. Wang, Y. Liu, W. Tan, *J. Am. Chem. Soc.* **2019**, *142*, 937.
[7] R. Yuan, Y. Li, Z. Wang, L. Jia, X. Guo, S. Zhou, *Nano Today* **2023**, *51*, 101899
[8] J. Yang, X. Lu, J.-L. Hao, L. Li, Y.-T. Ruan, X.-N. An, Q.-L. Huang, X.-M. Dong, P. Gao, *Nat. Commun.* **2025**, *16*, 1160.
[9] S. Tang, A. Fuß, Z. Fattahi, C. Culmsee, *Cell Death Dis.* **2024**, *15* .
[10] C. W. Brown, J. J. Amante, P. Chhoy, A. L. Elaimy, H. Liu, L. J. Zhu, C. E. Baer, S. J. Dixon, A. M. Mercurio, *Dev. Cell* **2019**, *51*, 575.
[11] Q. Feng, F. Qi, W. Fang, P. Hu, J. Shi, *J. Am. Chem. Soc.* **2024**, *146*, 32403
[12] S. He, J. Yu, M. Xu, C. Zhang, C. Xu, P. Cheng, K. Pu, *Angew. Chem., Int. Ed.* **2023**, *62*, 202310178.
[13] Z. Liu, S. Liu, B. Liu, Q. Meng, M. Yuan, X. Ma, J. Wang, P. ’. Ma, J. Lin, *Adv. Funct. Mater.* **2024**, *34*, 2407153
[14] J. B. Spinelli, M. C. Haigis, *Nat. Cell Biol.* **2018**, *20*, 745.
[15] Y. Liu, S. Lu, L. Wu, L. Yang, L. Yang, J. Wang, *Cell Death Dis.* **2023**, *14*, 519.
[16] D. R. Richardson, D. J. R. Lane, E. M. Becker, M. L.-H. Huang, M. Whitnall, Y. S. Rahmanto, A. D. Sheftel, P. Ponka, *Proc. Natl. Acad. Sci. USA* **2010**, *107*, 10775.
[17] S. Ben Zichri- David, L. Shkuri, T. Ast, *npj Metabolic Health and Disease* **2025**, *3*, 6.
[18] A. Suomalainen, J. Nunnari, *Cell* **2024**, *187*, 2601.
[19] D. C. Wallace, *Nat. Rev. Cancer* **2012**, *12*, 685.
[20] W. X. Zong, J. D. Rabinowitz, E. White, *Mol. Cell* **2016**, *61*, 667.

© 2025 Wiley-VCH GmbH

15214095, 0, Downloaded from https://advanced.onlinelibrary.wiley.com/doi/10.1002/adma.202508457 by University Of British Columbia, Wiley Online Library on [01/09/2025]. See the Terms and Conditions (https://onlinelibrary.wiley.com/terms-and-conditions) on Wiley Online Library for rules of use; OA articles are governed by the applicable Creative Commons License

[21] E. L. Mills, B. Kelly, L. A. J. O'Neill, *Nat. Immunol.* **2017**, *18*, 488.
[22] E. Vringer, S. W. G. Tait, *Cell Death Differ.* **2022**, *30* .
[23] M. M. Hu, H. B. Shu, *Cell Mol. Immunol.* **2023**, *20*, 1403.
[24] K. C. Mangalhara, S. K. Varanasi, M. A. Johnson, M. J. Burns, G. R. Rojas, *Science* **2023**, *381*, 1316.
[25] S. Marchi, E. Guilbaud, S. W. G. Tait, T. Yamazaki, L. Galluzzi, *Nat. Rev. Immunol.* **2022**, *23*, 159.
[26] J. Yang, T. Su, Q. Wang, R. Shi, J. Ding, X. Chen, *Adv. Mater.* **2025**, *37*, 2419033.
[27] P. Zheng, B. Ding, R. Shi, Z. Jiang, W. Xu, G. Li, J. Ding, X. Chen, *Adv. Mater.* **2021**, *33*, 2007426.
[28] J. Liu, Y. Yan, Y. Zhang, X. Pan, H. Xia, J. Zhou, F. Wan, X. Huang, W. Zhang, Q. Zhang, B. Chen, Y. Wang, *J. Am. Chem. Soc.* **2024**, *146*, 34568
[29] T. Zhang, L. Sun, Y. Hao, C. Suo, S. Shen, H. Wei, W. Ma, P. Zhang, T. Wang, X. Gu, S.-T. Li, Z. Chen, R. Yan, Y. Zhang, Y. Cai, R. Zhou, W. Jia, F. Huang, P. Gao, H. Zhang, *Nature Cancer* **2021**, *3*, 75.
[30] H. N. Munro, M. C. Linder, *Physiol. Rev.* **1978**, *58*, 317.
[31] B. Zhang, G. Tang, J. He, X. Yan, K. Fan, *Adv. Drug Delivery Rev.* **2021**, *176*, 113892
[32] Y. Y. Zhang, Y. Han, W. N. Li, R. H. Xu, H. Q. Ju, *Trends Pharmacol. Sci.* **2024**, *45*, 145.
[33] B. Galy, M. Conrad, M. Muckenthaler, *Nat. Rev. Mol. Cell Biol.* **2023**, *25*, 133.
[34] C. Zhang, S. He, Z. Zeng, P. Cheng, K. Pu, *Angew. Chem., Int. Ed.* **2021**, *61*, 202114957.
[35] W. Su, M. Tan, Z. Wang, J. Zhang, W. Huang, H. Song, X. Wang, H. Ran, Y. Gao, G. Nie, H. Wang, *Angew. Chem., Int. Ed.* **2023**, *62*, 202218128.
[36] Y. Chen, W. Li, S. Kwon, Y. Wang, Z. Li, Q. Hu, *J. Am. Chem. Soc.* **2023**, *145*, 9815.
[37] Q. Ma, H. Jiang, L. Ma, G. Zhao, Q. Xu, D. Guo, N. He, H. Liu, Z. Meng, J. Liu, L. Zhu, Q. Lin, X. Wu, M. Li, S. Luo, J. Fang, Z. Lu, *Proc. Natl. Acad. Sci. USA* **2023**, *120*, 2209435120
[38] C. K. Huang, Y. Sun, L. Lv, Y. Ping, *Molecular Therapy – Oncolytics 24*, **2022**: 288.
[39] B. Galy, D. Ferring-Appel, S. W. Sauer, S. Kaden, S. Lyoumi, H. Puy, S. Kölker, H.-J. Gröne, M. W. Hentze, *Cell Metab.* **2010**, *12*, 194.
[40] A. Martelli, S. Schmucker, L. Reutenauer, J. R. R. Mathieu, C. Peyssonnaux, Z. Karim, H. Puy, B. Galy, M. W. Hentze, H. Puccio, *Cell Metab.* **2015**, *21*, 311.
[41] X.-K. Jin, S.-K. Zhang, S.-M. Zhang, J.-L. Liang, X. Yan, Y.-T. Lin, R. Meng, Z.-H. Xu, C.-J. Liu, X.-Z. Zhang, *Adv. Mater.* **2025**, *37*, 2410957
[42] X.-K. Jin, S.-M. Zhang, J.-L. Liang, S.-K. Zhang, Y.-T. Qin, Q.-X. Huang, C.-J. Liu, X.-Z. Zhang, *Adv. Mater.* **2023**, *36*, 2309094
[43] A. Vogel, T. Meyer, G. Sapisochin, R. Salem, A. Saborowski, *Lancet* **2022**, *400*, 1345.

© 2025 Wiley-VCH GmbH

15214095, 0, Downloaded from https://advanced.onlinelibrary.wiley.com/doi/10.1002/adma.202508457 by University Of British Columbia, Wiley Online Library on [01/09/2025]. See the Terms and Conditions (https://onlinelibrary.wiley.com/terms-and-conditions) on Wiley Online Library for rules of use; OA articles are governed by the applicable Creative Commons License